

Scientific support for future space missions and multimethodological analysis of surface properties of solar system bodies

Auteur : Romagnolo, Amedeo

Promoteur(s) : Hubert, Benoit; 8567

Faculté : Faculté des Sciences

Diplôme : Master en sciences spatiales, à finalité spécialisée

Année académique : 2018-2019

URI/URL : <http://hdl.handle.net/2268.2/8386>

Avertissement à l'attention des usagers :

Tous les documents placés en accès ouvert sur le site le site MatheO sont protégés par le droit d'auteur. Conformément aux principes énoncés par la "Budapest Open Access Initiative"(BOAI, 2002), l'utilisateur du site peut lire, télécharger, copier, transmettre, imprimer, chercher ou faire un lien vers le texte intégral de ces documents, les disséquer pour les indexer, s'en servir de données pour un logiciel, ou s'en servir à toute autre fin légale (ou prévue par la réglementation relative au droit d'auteur). Toute utilisation du document à des fins commerciales est strictement interdite.

Par ailleurs, l'utilisateur s'engage à respecter les droits moraux de l'auteur, principalement le droit à l'intégrité de l'oeuvre et le droit de paternité et ce dans toute utilisation que l'utilisateur entreprend. Ainsi, à titre d'exemple, lorsqu'il reproduira un document par extrait ou dans son intégralité, l'utilisateur citera de manière complète les sources telles que mentionnées ci-dessus. Toute utilisation non explicitement autorisée ci-avant (telle que par exemple, la modification du document ou son résumé) nécessite l'autorisation préalable et expresse des auteurs ou de leurs ayants droit.

Scientific support for future space missions and
multimethodological analysis of surface properties
of solar system bodies

Master Thesis

Sunday 15th September, 2019



MASTER DEGREE OF SPACE SCIENCES

Author

Amedeo Romagnolo
(Student ID: 176733)

Internal Supervisors

Prof. Benoit Hubert
Prof. Denis Grodent

External Supervisor

Dr. Ozgur Karatekin

Examiners

Prof. Véronique Dehant Prof. Emmanuël Jehin

Ai miei nonni.

Non passa giorno senza che non vi pensi.

Se esiste qualcosa al di là di questa vita spero che possiate vedermi ed essere orgliosi della persona che sono diventato.

Mi mancate immensamente.

Abstract

This thesis will include the two main projects collaborations done at the Royal Observatory of Belgium (ROB) as part of the internship started in March and lasted until mid-August 2019.

The first project, with the collaboration of the *Institut royal d'Aéronomie Spatiale de Belgique* (BIRA-IASB), regarded the development of a data processing software to be used in the VIS-NIR detectors characterization for the Moon and Jupiter Imaging Spectrometer (MAJIS), which is one of the ten instruments constituting the ESA JUICE mission's science payload.

After a period of familiarization with Python programming language and a baseline software developed by ROB for UV observations, the data processing software was adopted to fully analyze and process the images from the MAJIS detector characterization. The validation of the software had been proved both by simulations from a model in collaboration with ROB, and (partially) by instrumental images obtained from the *Institut d'Astrophysique Spatiale* (IAS, France), which is leading the project.

The second project was aimed at improving the general knowledge of the planetary ice caps spectroscopic analysis via the study of Martian north pole; this has been done both to contribute to the understanding of the planet's climate via the analysis of the temporal evolution of H₂O and CO₂ polar ice, and to design a specific analysis software for spectroscopic data that could be used in the future for the MAJIS mission.

After a new familiarization period with MATLAB and the baseline scripts from previous works, a full software capable of processing spectroscopic data from the Compact Reconnaissance Imaging Spectrometer for Mars (CRISM) and monitoring the seasonal variations of the H₂O and CO₂ polar surface ice has been developed. The software has been partially validated with the literature, and the results suggest that an improvement has been done from the previous works in terms of processing time and noise reduction.

Both the projects provided enough scientific data for a co-authorship into two different posters for the EPSC-DPS Joint Meeting 2019 in Geneva, Switzerland.

Contents

1	MAJIS Data Processing Software	1
1.1	Introduction	1
1.2	The MAJIS experiment	2
1.2.1	Jupiter	2
1.2.2	Europa, Ganymede and Callisto	3
1.2.3	Io, Rings and Small Satellites	3
1.3	The Spectrometer	4
1.3.1	Optical Design	5
1.3.2	Spectral Performances	5
1.3.3	Dichroic	6
1.3.4	Gratings	7
1.3.5	Scan Mirror Unit	7
1.3.6	Internal Calibration Unit	8
1.3.7	Teledyne Detectors	8
1.3.8	Focal Planes	8
1.4	The VIS-NIR Detectors Characterization	9
1.4.1	The Facility	9
1.4.2	The Configurations	10
1.5	Characterization Procedure	11
1.5.1	Photon Transfer Curve	12
1.6	Characterization Parameters in Dark Conditions	14
1.6.1	Dark Current (DC)	14
1.6.2	Dark-Signal Non-Uniformity (DSNU)	15
1.6.3	Read-Out Noise (RON)	15
1.6.4	Power Dissipation	16
1.7	Characterization Parameters in Light Conditions	17
1.7.1	Useful Spectral Range	19
1.7.2	Quantum Efficiency	19
1.7.3	Full Well Capacity (FWC)	21
1.7.4	Saturation	21
1.7.5	Conversion Gain	21
1.7.6	Linearity	21
1.7.7	Defective Pixels and Cluster Mapping	23
1.7.8	Photo-Response Non-Uniformity (PRNU)	23
1.7.9	Operability	23
1.7.10	Persistence	24
1.7.11	Power Consumption	25

1.8	The Data Processing Software Development	26
1.8.1	The Baseline Software	26
1.8.2	The Work at ROB	26
1.9	Results	31
2	CRISM	35
2.1	Introduction	35
2.2	Introduction to Mars	36
2.3	The Instrument	38
2.3.1	Observations	39
2.4	Surface Ice Detection	41
2.5	Baseline Software	44
2.5.1	CRISM Software v2	44
2.5.2	CRISM Software v3	46
2.6	CRISM Software v4 Development	49
2.6.1	Scripts Improvement	49
2.6.2	Data Analysis	50
2.7	CRISM Analysis Results	53
3	Conclusions	56

List of Figures

1	Czerny-Turner Configuration	5
2	MAJIS Spectral Performances	6
3	Dichroic Efficiency	6
4	Gratings Efficiency	7
5	Characterization Bench	10
6	Characterization Measurements Diagram	11
7	Photon Transfer Curve	12
8	Non-Linearity Example	22
9	Short Wave Pass Filter	24
10	MAJIS Preliminary Simulations	27
11	Corrected PTC	28
12	Reference Columns Noise	29
13	Reference Columns	29
14	Corrected Reference Columns Noise	30
15	Reference Columns Signal after Subtraction	31
16	IAS-BIRA CDS Images Comparison	32
17	Simulated Defective Pixel Clusters	33
18	Simulated Persistence Pixel Color Map	34
19	Martian Solar Longitude	36
20	Martian Dust Annual Cycle	37
21	CRISM Components	38
22	CRISM Optics	38
23	IAS Simulated Spectra	41
24	Smile Effect	45
25	Noisy Mars Polar Cap	46
26	Noisy Mars Polar Cap Variability	47
27	CO ₂ ice from Brown et al.	48
28	CO ₂ ice from Piqueux et al.	48
29	Comparison of Noise Attenuation Methods	51
30	Perfect Sphere Distances Retrieval	52
31	Ice Caps Temporal Evolution	53
32	Complete Ice Caps Temporal Evolution	53
33	Areas Comparison of Ice Caps	54

List of Tables

1	Surface Ice Spectral Parameters	43
---	---	----

1 Data Processing Software for MAJIS VIS-NIR detectors

Acknowledgements: [BIRA] David Bolsée, Miriam Cisneros, Nuno Pereira, Gaël Cessateur; [ROB] Boris Giordanengo, Samuel Gissot, [IAS] Paolo Haffoud, François Poulet, Yves Langevin

1.1 Introduction

The Large Moons and Jupiter Imaging Spectrometer (MAJIS) is an instrument that will be part of the ESA Jupiter Icy Moons Explorer (JUICE), which is the first large-class mission of Cosmic Vision 2015-2025 [1].

The spacecraft is planned to be launched with either an Ariane 5 or an Ariane 64 launch vehicle in 2022 and reach Jupiter with gravity assist from Earth, Venus and Mars in 2029 [1, 2], with the goal of making detailed observation of the planet and its moons Ganymede, Callisto and Europa. The spacecraft will do several flybys around these bodies and will eventually insert in orbit around Ganymede. The mission will include ten state-of-the-art instruments and the spacecraft will host in its science payload eleven main experiments.

1.2 The MAJIS experiment

With the *Centre National d'Études Spatiales* (CNES, France) as the leading funding agency as the principal investigator, this experiment is a joint collaboration between several institutes, like the *Institut d'Astrophysique Spatiale* (IAS), the *Istituto Nazionale di Astrofisica* (INAS), the *Institut royal d'Aéronomie Spatiale de Belgique* (BIRA·IASB) [3], the *Royal Observatory of Belgium* (ROB) and the *University of Liège*.

1.2.1 Jupiter

With an IFOV of $125 \mu\text{rad}$ MAJIS will be able to have a resolution of 125 km from Ganymede's orbit [4]. In this conditions the full diameter of Jupiter will be continuously monitored with a coverage of 1070 pixels.

The orbit of JUICE will also enable MAJIS to take measurements of the planet's atmosphere in all local time conditions, not having therefore the coverage problems that JUNO had [4].

Below, the reader can find the MAJIS scientific objective for the planet's study.

- **Upper Atmosphere** - Since the instrument will be capable of detecting the H_3^+ bands around $3.7 \mu\text{m}$ [4, 5], which interact with Jovian auroras, MAJIS will be able to monitor auroral activity and phenomenology and to make instantaneous mapping.

In addition with stellar occultations one will be able to constrain methane mixing ratios in the stratosphere, and there will be the possibility to detect lightnings and night-glow emissions in the night-side hemisphere.

- **Troposphere** - In ideal cloud-free conditions, MAJIS will be able to compare the dynamical regimes associated with jet streams, plumes and storms occurrence at different altitudes to provide 3D dynamical scenarios.

Furthermore the instrument, via the detection of H_2O , NH_3 and NH_4SH ices, will provide constrains on convective motions. The considerably high data volume will allow researchers to monitor the behaviour and composition of hot spot regions.

- **Aerosol** - Thanks to JUICE orbit, MAJIS will not only be able to analyze the composition and size distribution of different cloud decks, but will even provide this data at several zenith angles, thus giving more insights about the condensation and photo-chemical phenomena originating aerosols.

1.2.2 Europa, Ganymede and Callisto

One of the main goals of the experiment is to get the surface composition of the Jovian satellites and to retrieve the non-ice materials distribution in function of geologic units at different scales.

Another main goal regarding the Jovian satellites is to spectroscopically analyze water ice in order to map its crystalline versus amorphous distribution and its average grain size. This will be extremely helpful to have a detailed mapping of the effects of the peculiar Ganymede's magnetic field and in general to both improve the amorphous ice models and to precisely determine the state of amorphous ice deposits. In addition, the retrieval of the different ices distribution will give great insights about the satellites' internal heat flux and cryovolcanism.

Finally, complementarily to the UV imaging spectrometer and particle instruments, MAJIS will perform "limb scans at high phase angles in order to highlight non-Local Thermodynamic Equilibrium (non-LTE) emissions of trace compounds"[4].

1.2.3 Io, Rings and Small Satellites

Since the mission design is for Ganymede, JUICE is not going to do close flybys around Io, but will instead "let some of its instruments to take remote measurements at a feasible distance" [4].

At a separation of 10^6 km MAJIS will still be able to study the moon volcanism and hemispheric thermal emission, and spectroscopically determine its superficial composition at regional scales with a resolution between 50 and 200 km/px [4]. These measurements will be probably done during Europa's flybys because of the spatial resolution requirements.

MAJIS will contribute to the 3D mapping of the Jovian ring particles' distribution and photometric behaviour at a wide range of solar phase angles and to analyze the bulk compositions of the small regular satellites revolving between 1.8 and 3.1 Jovian Radii.

1.3 The Spectrometer

MAJIS is constituted by a compact double channel spectrometer sharing one single telescope using a three mirrors anastigmatic system design.

The spectrometer has a single slit and the telescope is equipped with a pointing/scanning mirror. The VIS-NIR channel covers the range 0.4-2.35 μm , while the IR channel is between 2.25 μm and 5.54 μm , with a bridging region set at $1.7 \pm 0.2 \mu m$ [4].

The channels spectral samplings are 2.3 nm/band for the VIS-NIR channel and 6.6 nm/band for IR channel. With a Field of View (FOV) of 3.44° and a spatial resolution of 125 μrad /pixel [6, 5], the instrument will be able to cover from a distance of 500 km circular orbit over Ganymede a 30 km wide strip with a resolution of 62.5 m/pixel [3]. For observations of the atmosphere of Jupiter, instead, the radius of the circular orbit will be instead of 125 km.

In the two channels, a set of two Teledyne HgCdTe detectors is used to build the focal planes. Their instantaneous acquisition consists of the slit image, while multiple acquisitions contribute to build a *data cube* (3D data) set that associates a spectrum with each pixel on the ground. More into detail, since the two channels work simultaneously, the instrument will be able to give to each pixel a 0.4-5.54 μm spectrum. However, the detector is preceded by a Linear Variable Filter that allows MAJIS to operate both in scanning and pushbroom modes, depending on the requirements for the different phases of the mission.

In the following sub-chapters an overall look of the hardware used will be shown to have a qualitative comprehension of MAJIS operation.

1.3.1 Optical Design

The configuration used for the spectrometers is the Czerny-Turner with two plane gratings [4]. This configuration, visible in Figure 1, makes the light pass through a slit (B) and reflect on a curved mirror (C), which collimates it. After this step the radiation will be diffracted by a grating (D) and reflected on another mirror, which will refocus it on the exit slit (F) [7].

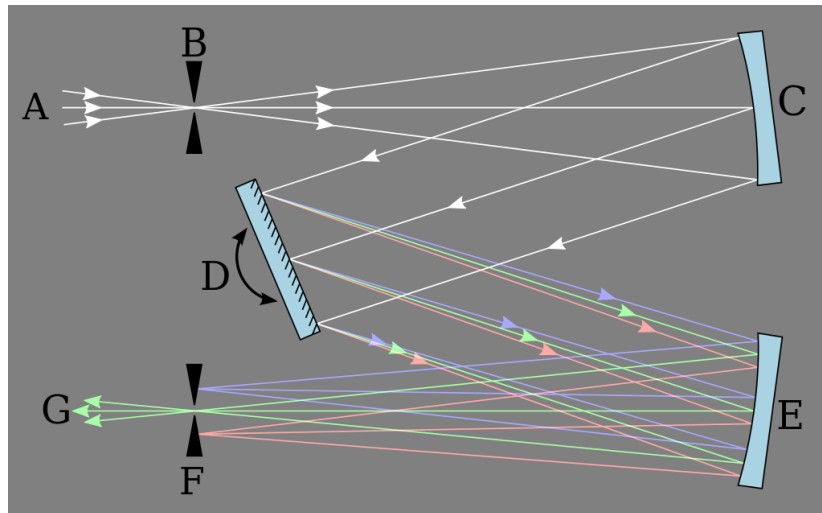


Figure 1: Default Czerny-Turner configuration [7].

As shown in the optical design includes a dichroic beamsplitter that divides the radiation between the two channels. This component has been created with the purpose of reflecting as efficiently as possible all the incoming radiation with a wavelength below $1.5 \mu m$ (VIS-NIR) and transmitting the wavelengths above $1.9 \mu m$ (IR). The spectral region between these extremes is part of both channels, and is considered of a great use for inter-calibration [3].

1.3.2 Spectral Performances

The design of the spectrometer has a strong impact on the spectral resolution of the instrument. Both channels have an almost constant value for the pixel spectral sampling, with better performances for the IR channels. Figure 2 shows the plots of this pixel sampling in function of the number of pixels. For the VIS-NIR band the sampling varies between 1.9 and 2.5 nm/pixel, while for the IR it is between 5.84 and 6.02.

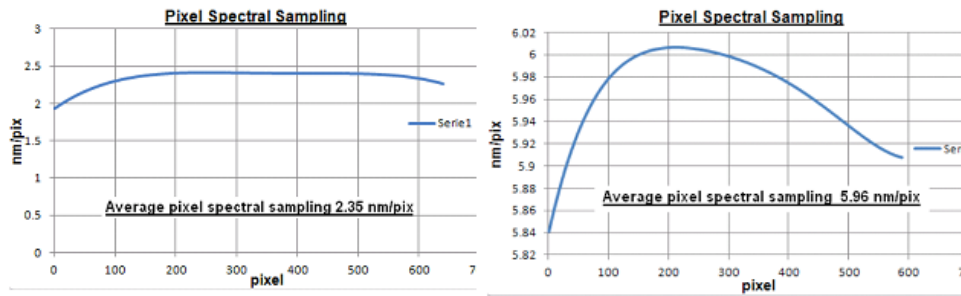


Figure 2: Spectral performances for VIS-NIR (left) and IR (right) [4].

1.3.3 Dichroic

As previously stated this element will have different behaviours with respect of the wavelength of the incident radiation. As one can see from Figure 3 the transmission and reflection values change noticeably for each channel. The moderate steepness of both transmission and efficiency parameters in the 1.4-1.9 μm range has been deliberately chosen in order to partially get the signal in both spectral channels.

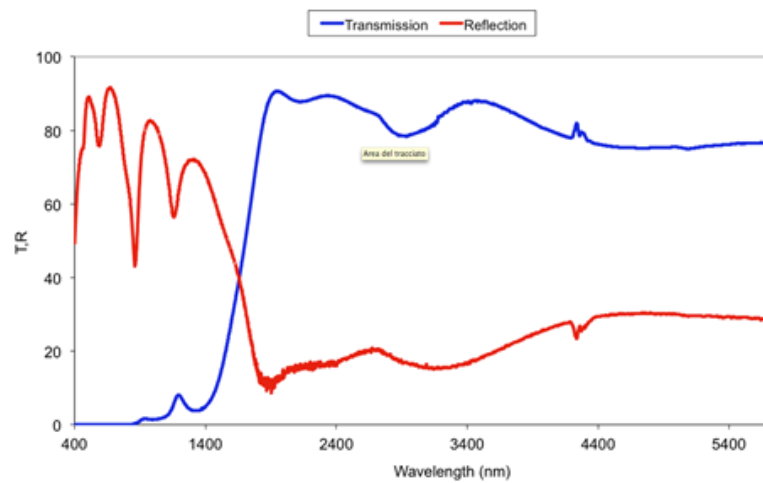


Figure 3: Tested dichroic efficiency in transmission for a ZnSe test substrate. "The spikes are due either to instrument or atmospheric ill-compensated features." [4]

1.3.4 Gratings

Customized gratings to maximize the performances along the considered bands. In Figure 4 one can find the preliminary measurements of this parameter in function of the wavelength for both channels.

The required formula to retrieve its value is determined by the ratio between the diffracted power and the incident one:

$$\eta = \frac{P}{P_0} \quad (1)$$

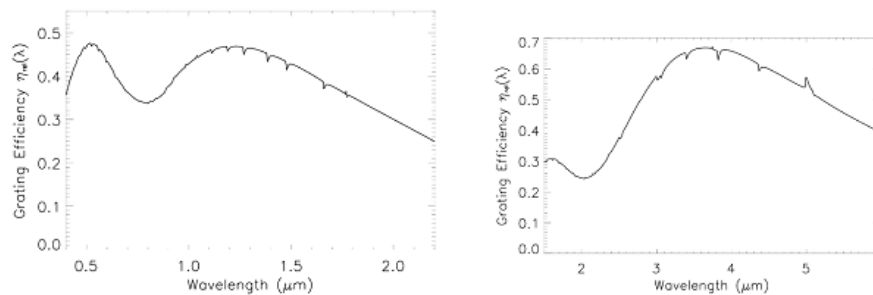


Figure 4: Preliminary evaluation of gratings efficiency for the VIS-NIR (left) and IR channels (right) [4].

1.3.5 Scan Mirror Unit

This element has two functionalities[3]:

- When the relative speed between the target and MAJIS is too low, it can retrieve a 2D image with similar spatial resolution for both considered directions, i.e. along and across the slit; the latter corresponding to the scan direction.
- When the relative speed is too high, with the assistance of a motion compensation mode it is capable to virtually increase the dwell time.

1.3.6 Internal Calibration Unit

The Internal Calibration Unit (ICU) is a subsystem integrated in the telescope's baffle. In this unit a diffusive element is illuminated by either an incandescence lamp or a IR source. Both are already calibrated, controlled in current and they are optimized respectively for the short and the long channel.

The light will then pass through a collimator and be reflected by a mobile scanning/pointing in the direction of the ICU optical axis. In this way it's possible to match the telescope and the ICU pupils and therefore illuminate the spectrometer's slit with a homogeneous reference signal. Some of the in-flight checks that are possible with this unit are [4]:

- Evolution of defective and non-linear pixels
- Spectral calibration
- Homogeneity of the flat-field
- Radiometric and linearity response stability

With periodical measurements made with ICU it will be possible to monitor aging, radiation and thermal degradation. A redundancy of the sources will help to remove ambiguity in case of deterioration [3].

1.3.7 Teledyne Detectors

Teledyne Technologies Inc. is a globally operating American industrial conglomerate that specializes in top-rank engineering [9]. For the MAJIS mission its high performance infrared detectors were chosen for the measurements.

These 1024×1024 pixels detectors are hybrid CMOS arrays, with a silicon-integrated circuit for signal readout and made with a HgCdTe crystal. Their peculiarity is that there is almost a linear correlation between ratio of cadmium (and similarly mercury) and both bandgap energy and cutoff wavelength. This means that these detectors can be easily tunable to reach the mission requirements [3, 10].

1.3.8 Focal Planes

For each channel a separated focal plane is implemented where the respective detector is housed inside a thermo-mechanical structure. These housings are equipped with specific optical and mechanical elements that were designed, among the many goals, to maintain the required thermal and cleanliness condition, to suppress to zero-order light reflected by the gratings, to maintain the correct alignment between the focal plane and the spectrometer's optical beam [3].

Both VIS-NIR and IR Focal Planes, in addition to the aforementioned thermo-mechanical housing, are composed of a Teledyne detector, a CMOS read-out integrated unit, an electrical connection, and a Linear Variable Filter (LVF).

1.4 The VIS-NIR Detectors Characterization

The *Royal Observatory of Belgium* (ROB) and the *Institut royal d'Aéronomie Spatiale de Belgique* (BIRA-IASB) are contributing to MAJIS with the characterization of VIS-NIR detectors, including the design and development of the bench at BIRA-IASB [12, 13].

To reach the requirements established by the MAJIS team, the facility was developed at a dark clean room class 100 and the instrument components were left at an operating temperature range between 116 and 160 K (liquid He closed cycle cooling) and in vacuum conditions ($<10^{-5}$ mbar).

It's extremely important for the team to precisely control illumination conditions, beam uniformity, exposure time, and/or data acquisition procedure. Three different configurations, described in section 1.4.2, were therefore defined to meet these needs.

The images taken in these three configuration will have then to be processed by an ad-hoc software to compensate for the noise and to retrieve the parameters (listed in section 1.5) that are required for the characterization.

1.4.1 The Facility

For the process, a characterization bench for the VIS-NIR detectors was built. Like the reader can see in Figure 5, at the beginning of the bench a light source is set to produce homogeneous radiation, which will then pass through a condenser and a movable cold plate.

The radiation will then be focused, filtered and modulated by the successive components of the bench and if the electronic shutter will be open, it will enter through a slit in the first monochromator. There the light will be diffracted through a series of mirrors and a gratings turret, and will afterwards pass through a slit into the second monochromator, where, after being further diffracted with a gratings turret, a flip mirror will determine if the light will end on a PbS/Si detector or will pass with an optical fiber to an integrating sphere. In the second case, the light will see the effects of its direction homogenized inside the sphere [14]. In this way the light will arrive at the calibrated PbS/Si and InGaAs detectors, and at the focusing array without any loss of information.

The light passing through the focusing array will then be focused on the Focal Plane Assembly (FPA) and enter the cooled vacuum chamber, where, if not stopped by the movable cold plate inside, it will be detected by the instrument inside the radiation shield. The plate is meant to be cooled down to avoid noise in the IR.

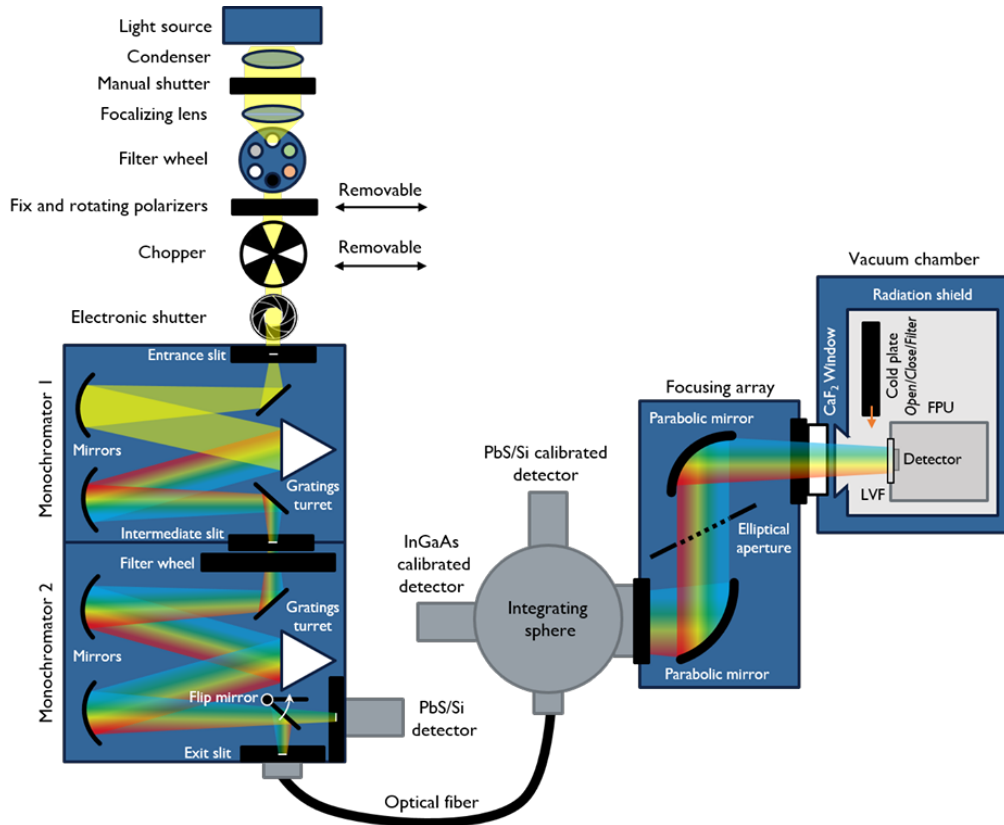


Figure 5: MAJIS VIS-NIR detector characterization bench [15] at configuration 3.

1.4.2 The Configurations

Taking as a reference Figure 5, the **first configuration** is simply about taking measurements with the movable cold plate in closed position in order to retrieve information in dark conditions. The **second configuration** uses instead the integrating sphere without the focusing array to provide uniform light over the surface detector, while the **third configuration** combines what is used in configuration 2 with a focusing array to simulate the convergence of the light beam as it will be produced by the block optics inside the MAJIS spectrometer. The description of their use and the characterization method will be described in greater detail in the sections 1.6 and 1.7.

1.5 Characterization Procedure

Note: The procedure has been defined by MAJIS team, IAS-ROB and IASB. For further details the reader can contact these institutes.

Despite the characterization is planned to start some weeks after the submission of this thesis, a clear definition of the procedures is almost complete. Figure 6 shows all the parameters (that will be described in the following pages) required for the characterization of MAJIS detectors, and explains all their measurable dependencies.

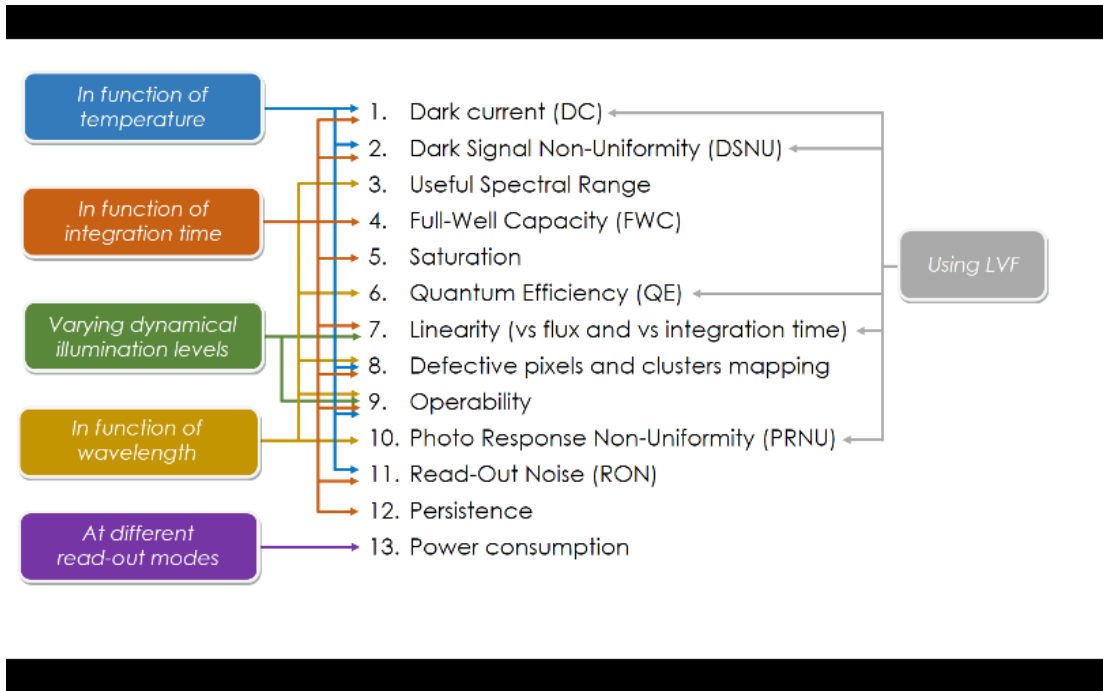


Figure 6: Characterization measurements diagram [16]*.

The procedure to perform the parameter measurements at **different temperatures**, will always start from the lowest to the highest value within the temperature test range (120K-150K), at intervals of 5K [16]*. In order to be sure that the detector is stable after the temperature change, the first three images (TBC) of every measurement will not be used in the data analysis. Additionally, during the characterization measurements, dark images, taken with the electronic shutter closed, will be obtained in order to be subtracted from the "light images" and removing therefore the background noise.

In a similar way, for the measurements taken at **different wavelengths**, the team planned a procedural increasing of from the shortest to the longest wavelength in the considered spectral range, in accordance with MAJIS spectral resolution [3]. A high amount of **different integration times** (IT) will be considered to range between the considered minimum and maximum values.

1.5.1 Photon Transfer Curve

The approach that has been chosen for the characterization of the detector is called *Photon Transfer Curve* (PTC), which is a standardized test procedure to provide "consistent, quantitative and verifiable performance data" [17].

The PTC basically stands on these three points:

1. The camera is a system block with light as an input and the digital data as an output.
2. The shot noise is the only noise produced by the input and its behaviour is easily predictable.
3. Any difference between the input noise and the output noise has been likely produced by the camera/sensors electronics.

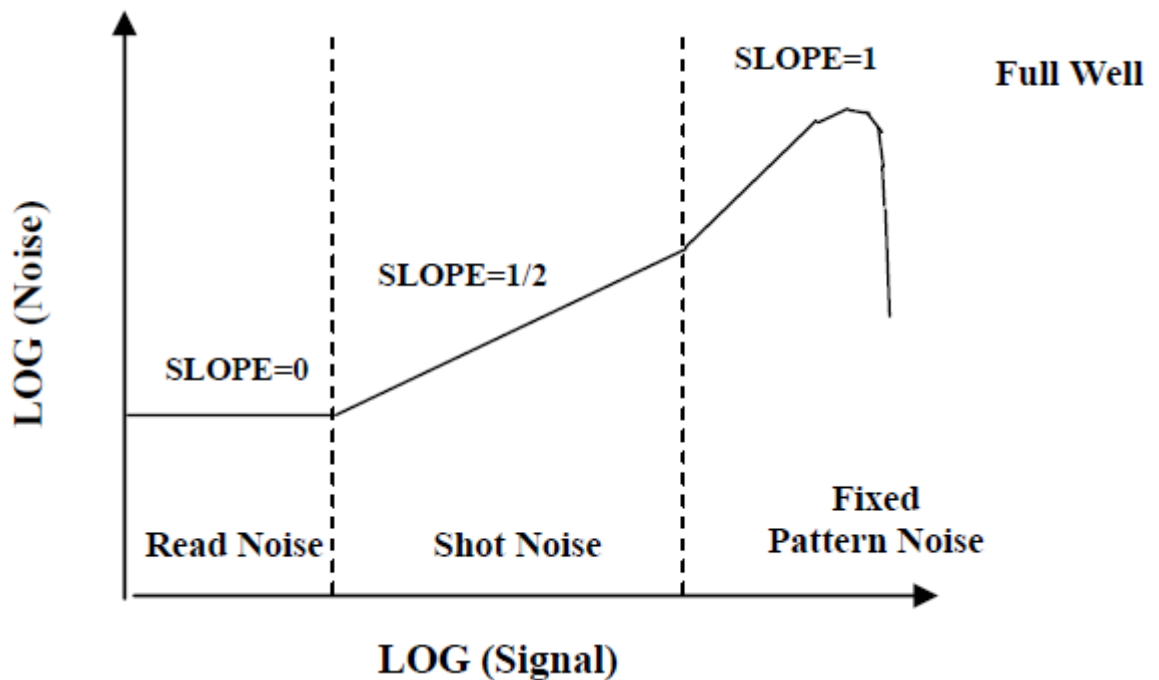


Figure 7: Photon Transfer Curve [17].

In Figure 7, representing the actual photon transfer curve with the logarithmic plot of the noise in function of the signal, three different kinds of noise are shown. The **read noise** is represented by the flat region at the leftmost area of the plot. This one is the random noise associated with the camera output amplifier and its external processing electronics. It is the baseline noise in total darkness and it doesn't have any dependency on the intensity of the signal.

The **shot noise**, instead, as shown before is the only one that doesn't originate from the camera and is inherent to light itself. Its root mean square value is equal to the square root of the mean number of photons incoming at each pixel, and therefore in the logarithmic plot shown in Figure 7 the linear correlation between the two values has a slope of $1/2$ [17].

Finally, **fixed pattern noise** is dependant on the sensitivity differences between pixels, or Photoresponse Nonuniformity (PRNU). It becomes the dominant noise in the Photon Transfer Curve only at high illuminations, and it is described by the following proportionality law [17]:

$$N_{FP} \propto (S \times PRNU) \quad (2)$$

Where N_{FP} is the fixed pattern noise, S is the signal, and PRNU is the Photon Response Non-Uniformity, which, as described in section 1.7.8, represents the difference between the output signal of the whole image and the one of the single pixels.

At this point, after a certain signal level, the output noise drastically decreases because charge sharing among pixels averages the signal and suppresses the random noise. At the peak where this phenomenon starts, the camera is said to have reached **Full well**. Usually cameras are calibrated in order to have their analog-to-digital (A/D) maximum output as close to this point as possible. In the following chapters the reader will see how this noise will be treated.

1.6 Characterization Parameters in Dark Conditions

According to the flux calculations performed during the design of the facility, a black-body at a temperature below 190K doesn't have a particular impact on the detector at NIR wavelengths. In configuration 1 the detector will face the cold plate surface (closed shutter) during the whole measurement procedure. The design of the radiation shield and the cold plate guarantees the absence of stray light beyond the shield itself. This procedure has been chosen by team among the several alternative because it better suits the characterization and the detector's requirements [16]*.

The characterization of the Maximum Integration Time (IT_{MAX}) of the detector is the following:

1. Set the optical bench to configuration 1.
2. Set the Focal Plane Assembly (FPA) at a given temperature.
3. Perform an acquisition at very large integration time and calculate the mean value of the matrix.
4. Periodically decrease the IT while taking new acquisitions and stop when the mean value is at 99% of the saturation level. This value will be considered the IT_{MAX} .

1.6.1 Dark Current (DC)

The DC is the thermal noise generated in semiconductor devices and it strongly depends on the temperature and the exposure time. Measuring the DC value for each pixel at the working temperature range of the detector will allow to determine the DC spatial uniformity on the detector matrix. In addition this will let the team to determine the offset signal obtained at zero integration time, which is by definition the Minimum Integration Time (IT_{min}).

The procedure to measure DC [16]* will involve setting the bench in configuration 1 and acquire images for a given temperature at a very large integration time, since the DC is supposed to increase with it, as described by the formula [18]:

$$\mu_d = \mu_{d,0} + \mu_{therm} = \mu_{d,0} + \mu_I IT \quad (3)$$

Where μ_d is the dark signal, $\mu_{d,0}$ is the one at $IT = 0$, and μ_{therm} is the thermally induced dark current, which can be expressed as a multiplying factor times the integration time.

The factor μ_I exponentially increases in function of the temperature [18]:

$$\mu_I = \mu_{I,ref} 2e^{\frac{T-T_{ref}}{T_d}} \quad (4)$$

Here T_d represents the "the temperature interval that causes a doubling of the dark current" [18], T_{ref} is a reference temperature with its reference noise $\mu_{I,ref}$.

After their retrieval, these images are averaged and the procedure starts again with increasingly lower integration times. The DC can then be measured either from the linear increase of these means or from the variance of the signal in function of the exposure time. The mean has been chosen for this purpose because of the better accuracy in its estimation.

1.6.2 Dark-Signal Non-Uniformity (DSNU)

This parameter represents the difference of the signal outputs between two different pixels in dark conditions and it constitutes, in addition to the Photo-Response Non-Uniformity (section 1.7.8), the fixed-pattern noise of the detector. To retrieve this value the first thing to do is to subtract, pixel by pixel, the averaged image at IT_{min} from the averaged images at higher ITs at a certain detector temperature to remove the noise. After that, the final step is using the following equation [16]*:

$$DSNU = \frac{Pixel\ signal - Average\ signal}{Average\ signal} \times 100\% \quad (5)$$

1.6.3 Read-Out Noise (RON)

It regards the additional noise introduced into an image when the value of a pixel is read and passes through an Analogical-Digital Converter (ADC) and an amplifier. Ideally this value should remain averagely constant, but in real conditions an image taken twice from the same pixel, random scatters will produce different results in terms of recorded ADU. In this situation RON therefore represents a measure of this scatter around the true signal value.

The procedure defined by the team to retrieve this parameter is to set the bench in configuration 1 and at a constant temperature to avoid noticeable fluctuations in the dark current and acquire several images at IT_{min} . After that, the procedure is repeated for different temperatures and the pixels' RON is finally determined from their standard deviation.

From this point, the defective pixels can be determined by the analysis of their signal value: if it's 90% higher than the average value they are then considered as defective and can be removed for a better analysis [3].

RON can finally be also determined using the PTC. In this way, it corresponds to the region below the non-linearity region at IT_{min} .

1.6.4 Power Dissipation

This parameters describes the energy per unit of time that is emitted by a device in operation. For VIS-NIR detectors it will vary in function of the power consumption of the heater at the copper plate. This parameter can be retrieved in two different ways.

The first one is to set again the bench in configuration 1 and to install all the components in the vacuum chamber unit. The heater of the copper plate is then supplied to reach the currents values that were retrieved in the power consumption characterization (Section 1.7.11) [16]*. After having heated the structural model until a stable detector temperature, the total power dissipation is represented by the power applied to the instrument.

Another way to retrieve this parameter is to measure the "output amplifier supply current and the capacitance of the clock gate electrodes" [20].

With this method it can be then calculated with the following equation [20]:

$$P = IV + CV^2\nu \quad (6)$$

With I representing the output amplifier supply current, V the voltage applied to the Read-Out Integrated Circuit (ROIC) [16]*, C the capacitance of each clock driver and ν the frequency for each clock driver.

1.7 Characterization Parameters in Light Conditions

To have measurements in this conditions, configurations 2 and 3 are used. In both cases the main system consists of a 1000 W quartz halogen acting as a light source in lamp housing and a double monochromator. The light source can cover the whole MAJIS spectral range, with a spectral irradiance close to a black-body emission around 3200 K [16]*.

The condenser of the lamp housing is coupled to a focalizing lens with same F-number (ratio between the system's focal length and the diameter of the entrance pupil) of the monochromator, which images the lamp filament on the entrance slit. With this method the monochromator provides a monochromatic beam at the output, which is tunable in wavelength. In addition, this provides a Full Width at Half Maximum (FWHM) that can be adjusted using the variable slits. The proposed sampling wavelength of 3.65 nm has been chosen because it corresponds to the bandpass of MAJIS VIS-NIR [16]*.

An external chopper placed between the filter wheel and the shutter allows to modulate the signal, setting therefore the system in Alternate Current mode (AC-mode). The monochromator allows instead to perform continuous-light acquisitions, and therefore Direct Current mode (DC-mode).

In these conditions two main properties are of vital importance: stability of the monochromatic beam and its calibration. Despite in theory their measurement should be independent of the working wavelength range, two couples composed by one calibrated and one uncalibrated detector each are used specifically for every considered wavelength range. For the VIS range there are two Si detectors, while for the NIR PbS detectors are used. Taking again as a reference Figure 5b, the uncalibrated detector will be placed on the auxiliary output port of the monochromator, while the calibrated detector on the port A of the integrating sphere and an InGaAs detector will be permanently placed in the port B. PbS detectors are calibrated and used exclusively in AC-mode because of its low phase sensitivity, while Si detectors can be used both in AC-mode and DC-mode. Finally the InGaAs is not calibrated in front of a primary source and can be used in both AC and DC modes.

Considering the illumination requirements for the FPA, in the VIS range the DC-mode will be adopted for both stability/calibration and FPA measurements while in the NIR range the team will use the AC-mode for the stability/calibration part and will work instead in DC-mode for the FPA measurements.

For the beam calibration, a proper **characterization of the difference in flux** between the port A and the FPA plane had to be done. The procedure, considering as usual Picture 5 as a reference, is fully described in the internal documentation [16]*. It will consist in setting the optical bench in either configuration 2 or 3 (depending on the test), placing the InGaAs detector (needed to monitor the stability of the light source) on the port B of the integrating sphere, the uncalibrated Si/PbS detector in the auxiliary output and the calibrated Si/PbS detector in the port A of the integrating sphere. The Si/PbS detector will then be moved from the integrating sphere to the FPA.

After some repetitions of this procedure, several signal values, both in dark conditions with the closed shutter and covering the whole MAJIS spectral range with the shutter open, will be acquired. In this way, results can be accumulated to calculate the required difference in optical power.

This characterization must be performed for both configuration 2 and 3.

After this, to get the **absolute calibration of the light beam** one has to set again the optical bench in configuration 2 or 3, and convert, for any FPA measurement at a given wavelength, the optical power previously retrieved in the integrating sphere into the optical power of the Focal Plane Assembly (FPA) with the application of a multiplicative factor representing the difference between the sphere and the FPA plane. This process is then repeated for all the whole MAJIS spectral range.

This calibration is mainly needed to determine the optical power in the FPA plane converted in irradiance (W/m^2) and the FPA signal once DC is subtracted, which in turn will be eventually used to compute the Quantum Efficiency (Section 1.7.2).

To retrieve instead the **relative calibration of the light beam**, an optical bench setting in configuration 2 is required. As for the case of the absolute calibration of the light beam, the optical power from the integrating sphere is converted with the correction factor into the optical power in the FPA plane with any measurement at a given wavelength. The FPA signal, after the DC subtraction, is then normalized with the previously calculated optical power. Like before, the process is then repeated for the whole MAJIS spectral range [16]*.

1.7.1 Useful Spectral Range

This parameter represents the wavelength range over which the detector is sensitive to. This means that the cut-off wavelength is defined as the 50% point of the relative peak spectral response. The required illumination is between 0.2 and 2.5 μm for this measurement.

After the calibration described in section 1.7, the FPA will be set at the operating temperature at which the lowest DC value was obtained. Several images will then be taken, for a specific IT, both in configuration 1 and with the detector illuminated at a given central wavelength. The procedure will be repeated until the whole wavelength range is covered. Finally, the acquisition of other images in configuration 1 is required, and optionally the whole process can be done for different FPA temperatures [16]*.

After the all the images for each wavelength are obtained, normalized for the constant optical power and averaged, the flux for each pixel in function of the wavelength is analyzed. The spectral ranges for each pixel will be therefore described by λ_1 and λ_2 , which are the extremes that define their flux FWHM.

1.7.2 Quantum Efficiency

The percentage of incident photons at a given wavelength (dark signal excluded) producing electrons in a semiconductors is represented by the quantum efficiency [16]*.

This parameter is described by the following formula [18]:

$$\eta(\lambda) = \frac{\mu_e}{\mu_p} \quad (7)$$

With $\eta(\lambda)$ as the total QE, μ_p the average photons number and μ_e the number of absorbed photons that produce electric signals.

As shown in equation 7 the QE is in function of the wavelength. This dependency can be explicitly seen in the formulation of μ_p [18]:

$$\mu_p = \frac{A * E * IT}{h\nu} = \frac{A * E * IT}{hc/\lambda} \quad (8)$$

Where A is the pixel area, E the irradiance, IT the integration time, and the denominator represent the energy of the photon, be it in function of the frequency or in function of the wavelength, with the planck constant and the light speed as multiplicative factors.

Among the several ways to measure it, for the MAJIS VIS-NIR characterization the team will isolate the whole detector surface from the light beam from the integrating sphere and illuminate the detector at the useful spectral range [16]*.

At this point, after the usual calibration, the FPA is set at an operating temperature that minimizes the DC value. Like for the useful spectral range, several images are taken both at configuration 1 and with the detector illuminated at a specific central wavelength, and after that the process is repeated for each wavelength in the considered range. Once all the wavelength has been covered, other final images are acquired in configuration 1 [16]*.

The images for each wavelength will then be averaged and corrected for their respective background noise. Finally a normalization for non-linearity effects will be applied. To determine the incident light flux over the detector, the PbS/Si calibrated detector in the secondary exit of the integrating sphere will be used. With all the results gained from the previous steps, the QE will be eventually calculated with the following equation [16]*:

$$QE = \frac{h \cdot c \cdot S_0}{G_S \cdot T_i \cdot E \cdot A \cdot \lambda} \quad (9)$$

Where h is the Planck constant [J·s], c the light speed [m/s], S_0 the average image signal after dark signal subtraction [ADU], G_S the overall system gain [ADU/e⁻], T_i the integration time [s], E the incident irradiance [W/m²], A the pixel area [m²] and λ the central wavelength of the considered spectral band [m]. If one instead wanted to calculate the per-pixel Response QE (RQE), the mean signal must be converted to equivalent electrons by the Sensor Chip Assembly (SCA) transimpedance gain (provided directly by Teledyne) and divided by the absolute number of photons in the signal.

1.7.3 Full Well Capacity (FWC)

This parameter can be described as the charge that the single pixel can hold before saturating. For this measurement a very stable flat field (configuration 2) is required.

The beginning of the characterization of this parameter will start by setting the FPA at a given temperature. Several images taken for one-hundred different IT intervals scaling from IT_{min} to IT_{MAX} will be taken at both configuration 1 and configuration 2. Finally this procedure will be repeated for different FPA temperatures .

From the linear regression of the acquired signal for each pixel, the point where the deviation exceeds 5% represents the FWC of the pixel [16]*.

1.7.4 Saturation

Saturation is indicative of the linearity degradation of the measurement in function of the IT. Saturation is defined as the maximum of the measured signal level of the detector.

FWC is normally higher than saturation because it corresponds to the physical saturation of the pixel [16]*.

1.7.5 Conversion Gain

Being the relationship between the ADU signal and incident electrons, it can be determined from the PTC. This parameter is indeed given by the slope of the linear regression in the shot noise-dominating region from the variance versus mean pixel value plot [16]*.

1.7.6 Linearity

The linearity error is defined as the discrepancy between the signal measurements and the linear fit obtained with respect to the input irradiance in the detector [16]*, or as the "maximal deviation and the minimal deviation in the range between 5% and 95% of the saturation capacity" [18].

Linearity can be measured in different ways, both in function of the IT and in function of the incident flux. In the case of the integration time the procedure is to set the monochromator at the central wavelength for which QE was measured to be the highest and set the FPA at a given temperature. Then several images, both in configuration 1 and with the detector illuminated at the aforementioned wavelength, will be acquired for different ITs ranging from IT_{min} to IT_{MAX} . The procedure will afterwards be repeated for other FPA temperatures [16]*.

Every set of images is finally corrected from the background image. The linearity is retrieved from the maximum absolute error obtained between each output value and the straight line fitted to the data. As previously mentioned, the linear range is the fraction over which the photometric responsivity is within 5% of the mean slope.

It's important to mention that, as partially shown in figure 8, which represents the plot of the measured signal and its linear fit in function of the IT, because of intrinsic features of the detector the measurements with an IT close to either zero or saturation tend to deviate more from the linearity than the rest of the data points. It is therefore crucial to "thicken" the considered set of integration times in these two specific areas.

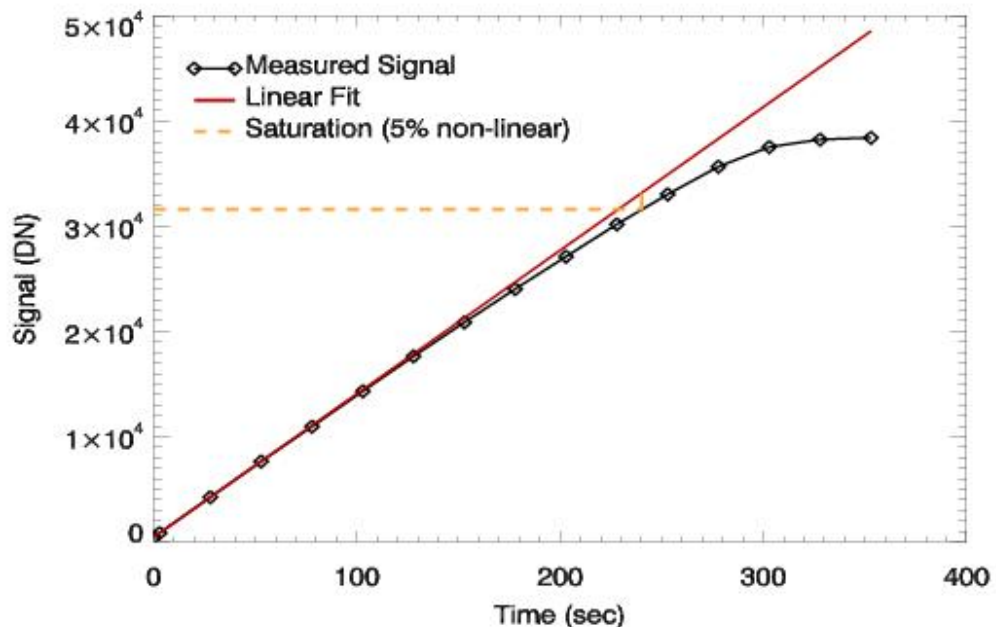


Figure 8: Non-linearity example from [19].

1.7.7 Defective Pixels and Cluster Mapping

Defective pixels include hot pixels, which have an extremely large and positive offset, and dead pixels, which have much lower sensitivity. For the characterization, logarithmic histograms will be used to identify the properties of the pixels, as well as pixels maps to identify the defective clusters than can be found in the detector [16]*.

The specifications describe a defective pixel as a pixel in a centered 800x1016 vertical window whose total dark signal exceeds 250 e⁻/pixel/s and has a QE<35% at the full wavelength range [16]*.

1.7.8 Photo-Response Non-Uniformity (PRNU)

Considering a uniform illumination and without any correction for defective pixels, PRNU corresponds to the output signal divergence between the whole image and the single pixels. Combined with the DSNU this parameter represents the fixed-pattern noise of the detector.

To retrieve it, the FPA must to be set at an operating temperature that produces the lowest DC possible. After that, a whole set of images at $IT_{MAX}/2$ must be taken at both configuration 1 and 2 for each wavelength in the considered range. Once this range will be fully covered, another set of images in configuration 1 will be covered.

Optionally, this procedure can be repeated for different FPA temperatures [16]*.

After the correction of the mean images with their corresponding background mean image the PRNU can be calculated with equation 5 in the same way it is done for DSNU [16]*.

1.7.9 Operability

The detector capability to keep working in functioning conditions is described by the operability. In these regards, every pixel is considered as defective and centered in the 800×1016 vertical window if [16]*:

- Its total dark signal exceeds 250 e⁻/pixel/s at the operating temperature.
- QE < 35% independent of the median value. The QE at 500 nm is not taken into account because Teledyne measurements showed that it's not representative of the overall efficiency.
- CDS noise is > 70 e⁻.

1.7.10 Persistence

This parameter is defined as the amount of residual photocharge left in a pixel from previous readouts. It is measured with pulsed illumination but in the case of NIR wavelengths there's the need to drastically reduce the black-body emission at that spectral range. With the use of the movable cold plate and the short wave pass filter, which is used to remove the black-body radiation from the window after closing the electronic shutter, this emissions coming from the CaF_2 becomes negligible [16]*. These filters are peculiar because they have an edge transmission coating on the front surface that reflects (relatively) longer wavelengths and instead transmits the shorter ones [21, 22]. Figure 9 is an exemplificative representation of the behaviour of a short wave pass filter, where the transmission almost constant in function of the wavelength with the sole exception of the range between 520 and 560 nm [22]. Despite the used filter is not from the same company and wasn't designed for the same wavelength range, its functioning is analogous.

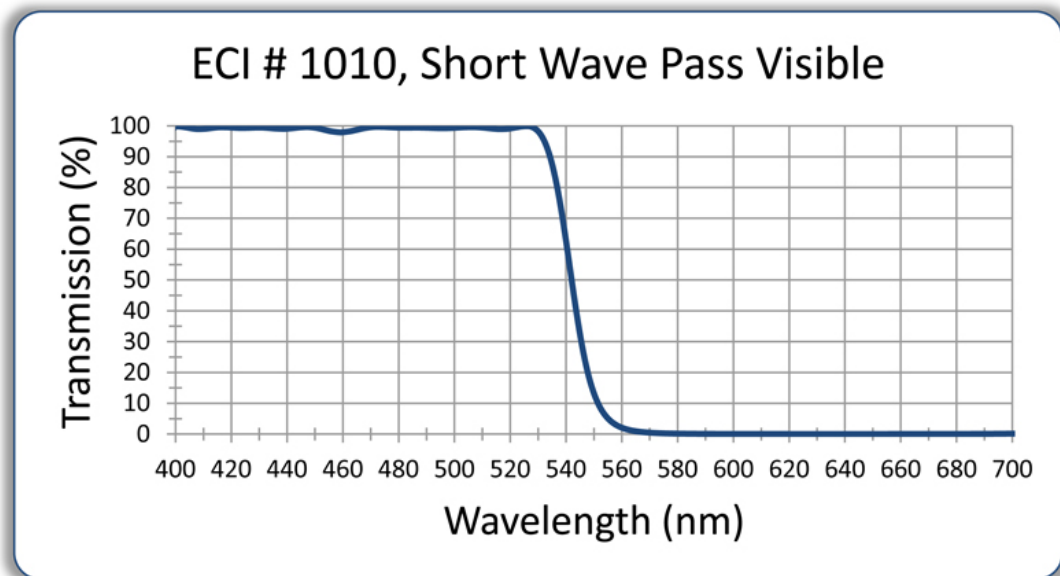


Figure 9: Example of the behaviour of a short wave pass filter in the visible range [22].

The procedure to determine this factor is to set again the FPA at a given temperature and place a short wave pass filter in front of the detector. Several images will be taken with the shutter at first open and then closed for a range of ITs ranging between IT_{min} and IT_{MAX} . The measurement process will be eventually repeated for different FPA temperatures [16]*.

Finally, the equation used to calculate this parameter is:

$$Persistence (\%) = \frac{Residual\ signal}{Useful\ signal} \times 100\% \quad (10)$$

To reduce the amount of pixel maps to process, an integration time binning is also planned. The size of this binning range will be defined during the characterization process in order to not be so extended to drastically alter the pixels response.

1.7.11 Power Consumption

The power consumption represent, as the name suggests, the required energy per units of time to be supplied for the functioning of a specific device. To determine this factor one has to set the FPA at lowest DC temperature and acquire some images in configuration 1 at a specific IT. The polarizers array will then be set at the position that allows the lowest possible illumination. This illumination will be set at the central wavelength that was measured to lead to the highest QE. Another round of image acquisitions will then be done and the data of current and power consumption provided by both electrical device and the current in the heaters of the copper plate will be saved. The procedure will be finally repeated with the polarizers array set in different positions to allow different levels of illumination, and optionally this measurement can be repeated again for different FPA temperatures.

1.8 The Data Processing Software Development

1.8.1 The Baseline Software

The team DeMeLab-STCL, which is part of the department of Solar Physics and Space Meteorology at ROB, developed in the past a baseline for a data processing software in Python that would have been used to characterize CMOS and APS sensors for the Extreme Ultraviolet Imager that will be used onboard the Solar Orbiter mission for Sun observations. For further details the reader can address the team via the submission of a formal request.

This software is mainly divided into four packages. The first one simulates a default scenario where a certain photon flux at a determined wavelength interacts with a detector, whose instrumental specifics are hard-coded. The output of this package is of a crucial importance because, in absence of real CDS measurements, it can be used for preliminary software training.

The second script regards instead a default preprocessing procedure to adapt both images and the data to be finally processed by the other two packages.

The third one retrieves the photon transfer curve, all the parameters in dark conditions, the full-well capacity and the linearity can be retrieved, while the last one detects directly the defective pixels in the sensor.

All the outputs of these packages are images in the Flexible Image Transport System (FITS) format. These files are very useful because, besides the image itself, they even an ASCII header that the users can read to investigate the metadata, like in this case the user's name, the IT, the temperature, the wavelength, etc. Furthermore, a .json (JavaScript Object Notation) document containing all the important data from the .fits header, is automatically generated at each run of the packages.

1.8.2 The Work at ROB

As previously mentioned, the baseline software provided by ROB needed to be updated and modified to fit the goal of the mission. First of all, after a period of familiarization with the scripts and with Python programming, both hard-coded data regarding the detector properties and the scripts inside the simulation package were adapted to properly simulate a situation similar to the one that can happen on the VIS-NIR detector during the characterization.

The code was initially simulating the non-linearity via normal distribution, which would have led, in the case of MAJIS detectors, to have a higher deviation from linearity in those regions where it should instead be more linear.

An arcsin distribution, or even an ad-hoc function to properly distribute the linearity in a way that linear the central part of the fitted line linear and make the two extremes has been proposed.

Finally, the default package simulated the images in function of the integration time with a logarithmic distribution. While this choice would have been adequate for the lowest ITs, this would have meant very few images in proximity of the saturation. Because of the non-linear behaviour of the PTC with the integration time close to both zero and the full well, the team requires a high amount of data in these two specific areas, and therefore a linear distribution of the ITs has been implemented to better simulate the required dataset.

After the simulations package was adapted to fit the characterization requirements, a first training campaign begun with the new synthetic data to validate the preliminary part of the software.

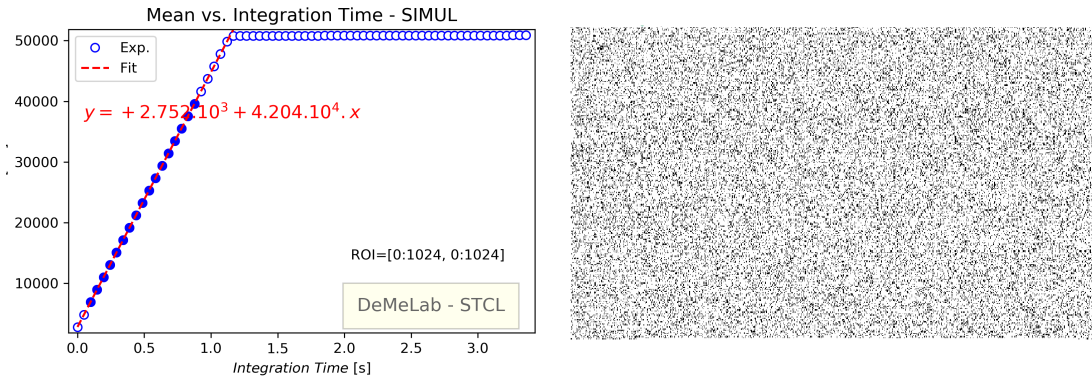


Figure 10: Preliminary training with the simulations from the adapted software, with a completely linear dataset before the full well. On the left: PTC curve with the data (in DN) reaching the Full Well. On the right: Defective pixels representation. Full dots represent the data points used to make the fit of the line.

Figure 10 shows the results of the first training campaign. On the left the reader can see the representation of a Photon Transfer Curve, in terms of the averaged signal (in DN) in function of Integration Time, which arrives at the instrumental saturation. For simplicity in a first moment the non-linearity has been simulated to be close to zero. On the right instead a map of the defective pixels has been represented. In the simulations, the presence of both dead and hot pixels has been arbitrarily set via a Poisson distribution.

The problem with these simulations was nevertheless the fact that the software creates images in the .fits format that are already a full developed image, while instead the problem is that in reality each image retrieved from the detector brings with itself the whole instrumental noise of each pixel, represented in Figure 7 by the fixed pattern noise. In order to avoid this noise to show up in the Photon Transfer Curve, a data reduction process needs to be implemented.

The way to suppress the fixed pattern noise is to take two consecutive images at the same integration time and subtract pixel-by-pixel one to the other one, since the fixed pattern variations are present in both pictures. In this way, as noticeable from Figure 11, representing the logarithmic plot of the noise in function of the signal, the shot noise area will extend until the full well. The read noise, being the noise floor of the camera, can be recorded in the PTC at a zero illumination level.

The validity of this method has been confirmed by a data training with Teledyne images that were kindly given by the IAS team in Paris. Unfortunately, the results of this process are not accessible for the public because of confidentiality agreements.

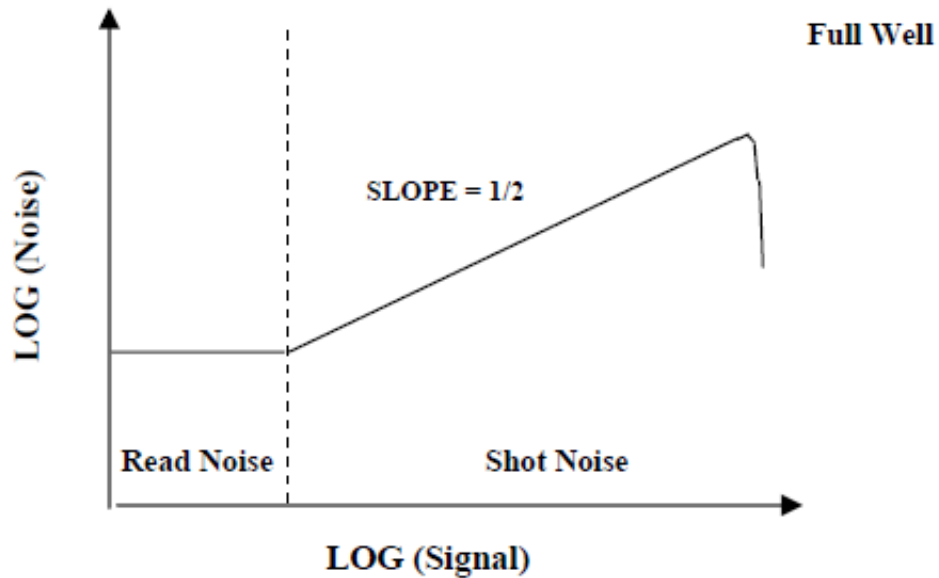


Figure 11: Photon Transfer Curve corrected for the fixed pattern noise [17].

Additionally, after this subtraction, except for the Correlated Double Sampling (CDS) noise no dark signal should have theoretically been present on the reference pixels, but a previous test campaign at IAS showed instead a noticeable signal along the reference pixel columns.

Figure 12 shows the measured dark signal by IAS for each pixel column of the detector. This divergence has been shown to be relative to the intrinsic properties of the detector. For further details of this newly discovered behaviour the reader can address the IAS team via the submission of a formal request.

This reset perturbation is highly visible on the reference pixels, but it's actually present on the whole CDS image.

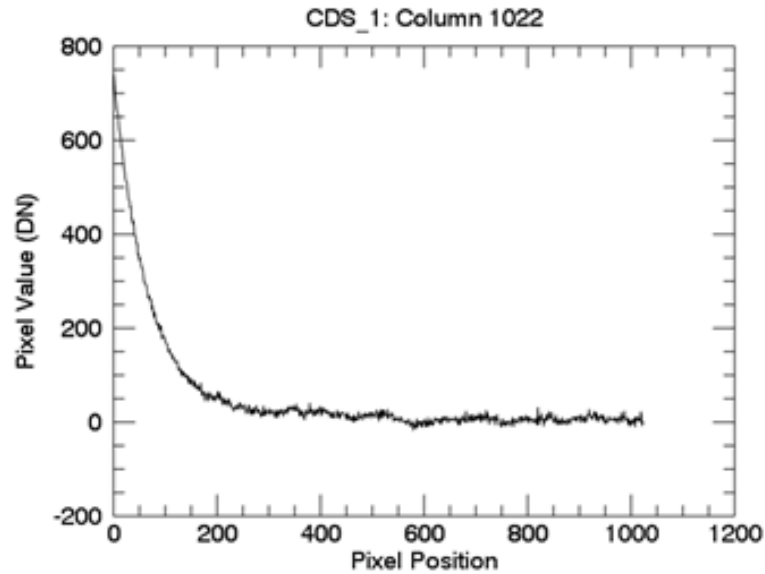


Figure 12: Detected noise on the reference pixel columns on the detector. Image kindly distributed from personal communications with Paolo Haffoud (IAS).

After a mission at the IAS in Paris on behalf of the Belgian team, among the different possible solutions in image processing to compensate for this perturbation, it was decided to compensate for this effect with the following procedure:

- Construct a matrix containing the pixel columns 1-4 and 1021-1024, representing the first and the last four detector columns, as shown in Figure 13. (The same operation can be done for the rows, instead).

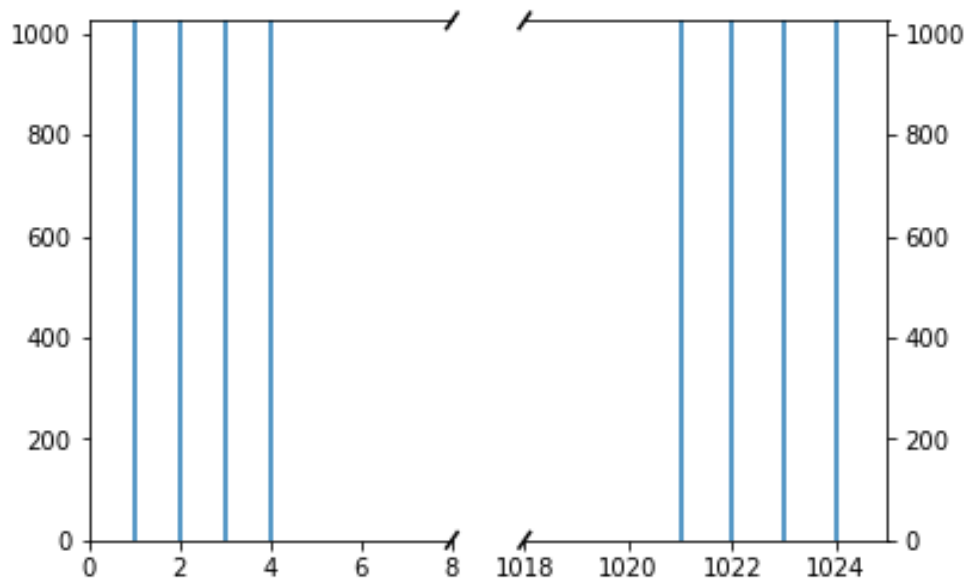


Figure 13: Reference columns in the 1024×1024 pixels detector that were used in the noise correction.

- Sort the pixels from each row of the new matrix and pick the four ones in the middle.
- Calculate all the average pixel values from the four pixels taken in each row.
- Subtract each retrieved mean pixel to the respective row of the whole detector.

Upon the implementation of this method in the characterization software, thanks to some preliminary dark images confidentially provided by IAS the column subtraction scripts were trained with real images (results in section 1.9), and a reference signal centered to zero, as the one required from the CDS requirements and shown in Figure 14, has been retrieved from the images.

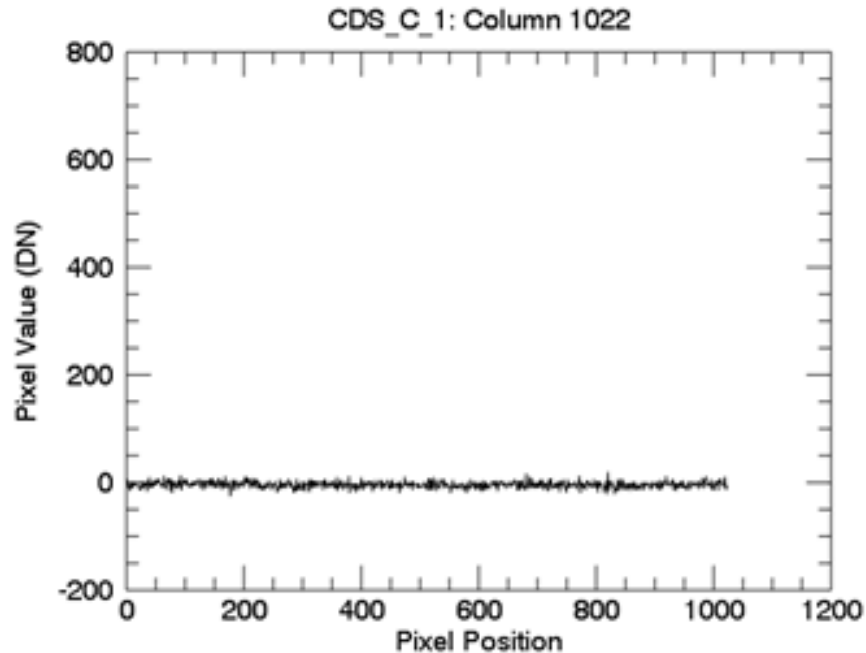


Figure 14: CDS signal after the processing correction. Image kindly distributed from personal communications with Paolo Haffoud (IAS).

Thanks to some preliminary dark images confidentially provided by IAS and the developed simulation package, the software so far could have been trained with both real and simulated images.

After the instrumental noise and perturbation subtraction has been implemented in the package, the second part of the data processing software development regarded at first the definition of a procedure to experimentally retrieve the required parameters, and then their implementation within the software. Once these steps were covered, a new package capable of retrieving the missing parameters for the characterization, i.e. useful spectral range, saturation, quantum efficiency and persistence has been delivered.

1.9 Results

At the end of the working period at ROB, a software capable of processing all the required parameters for the characterization mission has been delivered from the baseline ROB software.

The correct implementation of the subtraction method has been validated by the analysis of the post-subtraction reference columns, whose output images, as expected from the procedure and shown in Figure 15, have an average signal value close to zero.

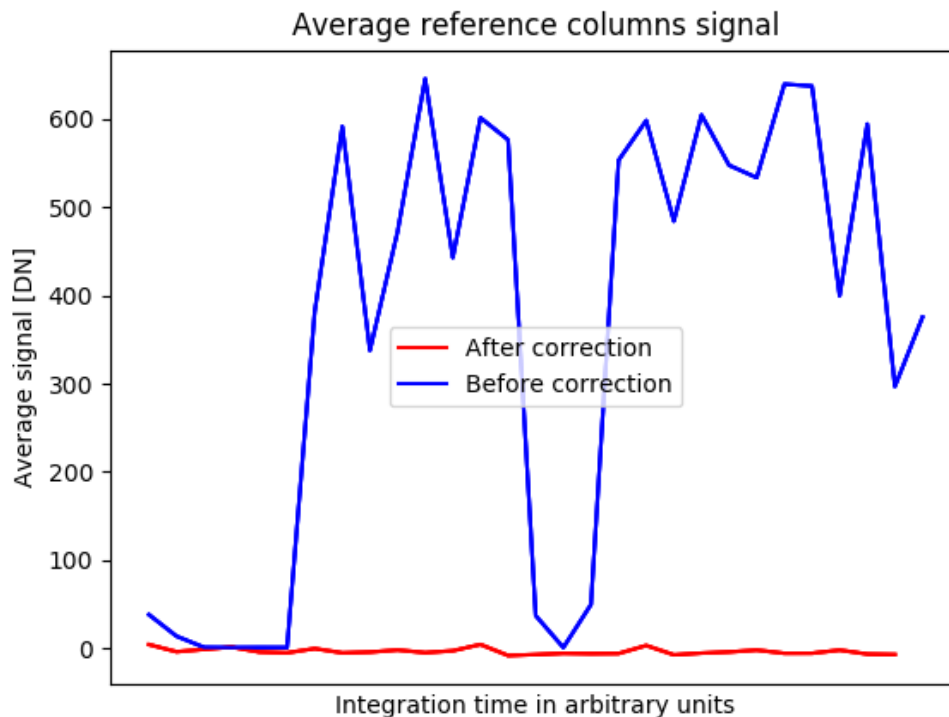


Figure 15: Average reference columns signal in function of the integration time.

As an additional proof of the correct implementation of the procedure, a comparison has been done between the processed CDS images from the developed software and the processed CDS images from the IAS code. Figure 16 is an example of the processed CDS images that were compared: on the left side the reader can see the output image from the IAS code, while on the right side the output image from the the software developed for the VIS-NIR detectors characterization.

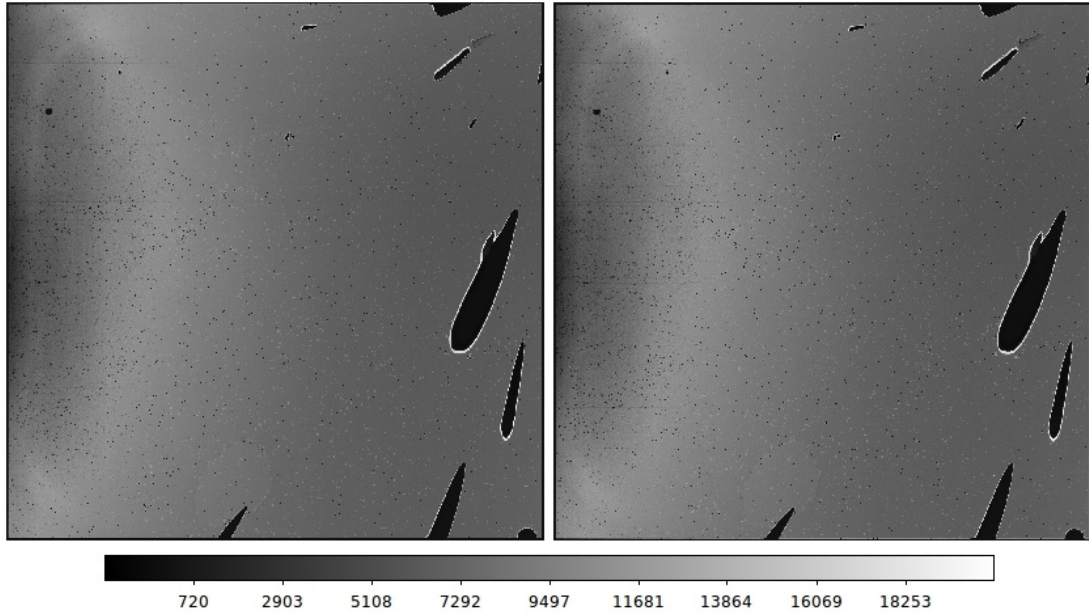


Figure 16: Comparison between the CDS images processed by the IAS software (on the left) and by the software developed in this work.

From the analysis of the average signal along the whole image (without the reference columns and rows), the comparison showed a percentage difference between the two images around 0.005%. This very small discrepancy is likely attributable to the fact that the IAS code was developed in IDL, whose decimal precision for float numbers is different from Python's.

All of the software packages were validated and trained via both simulated data and the dark images from the IAS laboratory.

The final outputs of the whole software are the following:

- **Dark Current (DC):** Saved in the final analysis of dark images as a [DN/s] numerical value. Retrieved from the analysis the dataset means in function of the integration times.
- **Dark Signal Non-Uniformity (DSNU):** Saved in the final analysis of dark images as a dimensionless numerical value.
- **Useful spectral range:** Since this parameter is pixel-dependent, a full table containing in each cell an array with both minimum and maximum wavelength for each pixel's useful spectral range has been implemented as an output.
- **Full-Well Capacity (FWC):** Retrievable in the linearity plot given during the PTC analysis. Evaluated as the first value in the PTC to deviate more than 5% from the linearity.

- **Saturation:** Saved in the final analysis of light images as a [DN] numerical value. Considered as the maximum value reached by the full well.
- **Quantum Efficiency (QE):** A table where the used central wavelengths and their relative quantum efficiencies is created.
- **Defective pixels:** Via the combination of both light and dark images, a full list of pixel maps, showing defective columns, defective rows and defective pixels is available. To retrieve the final defective pixels map, a step-by-step calculation using dark images, light images and the offsets has been used.
- **Cluster mapping:** In the same software package that retrieves the defective pixels, the defective clusters maps are drawn by considering adjacent defective pixels. Figure 17 shows the defective pixel clusters from the simulated data used to validate this part of the software. The color scale shows the efficiency, between 0% and 100%, of each pixel.

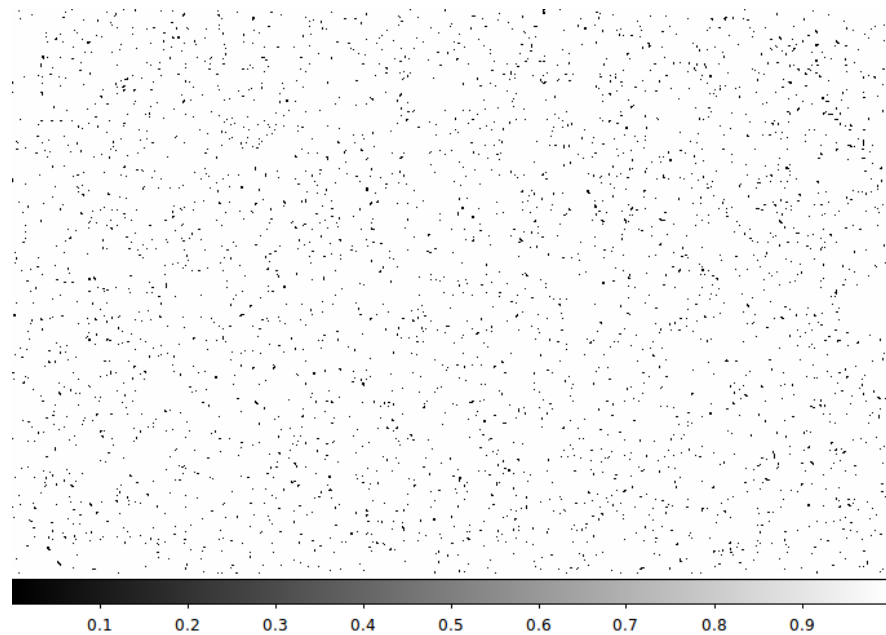


Figure 17: Simulated defective pixel cluster map.

- **Linearity:** In the light images analysis, a linearity plot under a 5% deviation can be retrieved.
- **Photo Response Non-Uniformity (PRNU):** Saved in the final analysis of light images as a dimensionless numerical value.
- **Read-Out Noise (RON):** Saved in the final analysis of light images as a dimensionless numerical value, and retrieved from the analysis of the dataset variances in function of the integration time.

- **Persistence:** Pixel color maps for each temperature and IT ranges are generated. A free parameter inside the code has been left for a potential binning of the integration times. For no binning, a dataset of simulated images with random pixel properties created a map like Figure 18.

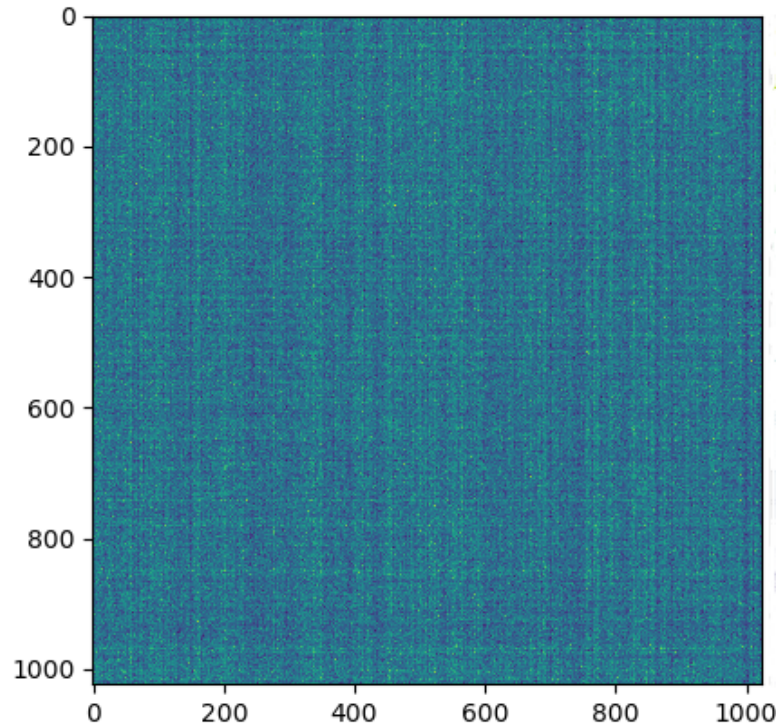


Figure 18: Simulated pixel color map for the persistence of each pixels. Color scale in arbitrary units.

As part of the software delivery, a user guide has been distributed to let the MAJIS team to operate the software as easily as possible has been delivered.

This work, in addition to the one of the whole MAJIS Belgian team, gave enough scientific and technical data to present a poster at the EPSC-DPS Joint Meeting 2019 in Geneva, Switzerland, which is entitled [13]:

EPSC-DPS2019-551

Validation tests of the calibration bench for the characterization of MAJIS/JUICE VIS-NIR detectors

by Miriam Estefanía Cisneros González et al.

Session MIT1 - Upcoming and Future Planetary Missions and Instrumentation

2 CRISM

Compact Reconnaissance Imaging Spectrometer for Mars

Acknowledgements: [ROB] Alfonso Caldiero, Luca Ruiz Zolano, Orkun Temel, Bart Van Hove, Grégoire Henry

2.1 Introduction

To properly understand the climate and the energy balance of Mars, a proper comprehension of the behaviour of its polar regions and the interactions between their sublimation/condensation cycle and the planet's atmosphere is required. As studies previously suggested [23], the CO₂/H₂O ice cycle may be changing over time and has therefore to be constantly monitored in order to get a proper understanding of its dynamics. This can be extremely useful for the surface mass distribution modelization of the planet, and therefore for its gravity field and rotation rate variations [24].

The Compact Reconnaissance Imaging Spectrometer for Mars (**CRISM**) is a VIS-NIR imaging spectrometer aboard the Mars Reconnaissance Orbiter (MRO) whose main objective is to detect mineralogical traces of past and present water on Mars.

One of the goals of the ROB Mars team, despite CRISM already has a freely available data analysis software, was to develop a software capable of analyzing the instrument's spectroscopic data regarding the planet's polar regions at different solar longitudes. This software has been in continuous development for more than three years mainly for the data from NOMAD mission, but it needed to be implemented for CRISM data and it had to show feasible results.

The following step, after the development of the software, was the comparison with the literature and the data obtained from other source. Upon the method validation the final goal was to effectively map the CO₂/H₂O surface ices on the north pole and study their evolution.

This software can be extremely helpful, with a relatively short adaptation work, for the data analysis of future spectroscopic missions that will aim at analyzing the temporal variation of surface ices on solar system bodies. As a matter of fact, one can easily deduce that the development of this software wasn't uniquely aimed at the analysis of Martian climate, but also for a future adaptation for the MAJIS measurements on the moons of Jupiter.

2.2 Introduction to Mars

Similarly to Venus, Mars has an atmosphere that is mainly composed by CO_2 , with low amounts of oxygen and water vapour (high variability). Since its surface pressure is as low as 610 Pa, the planet is not able to maintain a strong greenhouse effect. This leads to large diurnal temperature variations during the Martian day. In order to keep track of the events on Mars and facilitate data comparison, a whole set of temporal parameters has been defined. The beginning of the Martian calendar was set to start at the northern spring equinox of the 11th of April 1955 [26]. This means that, because of the divergence in the length of the sidereal year between the planet and Earth, nowadays (summer/fall 2019) we are in MY 35. The seasons, instead, are determined by the Solar Longitude (L_s) on the planet, which, as represented in Figure 19, represents the position of Mars relative to the Sun measured in degrees from the vernal equinox, when $L_s = 0$. According to the Mars Climate Database, the four seasons on Mars start with northern Spring for L_s between 0° and 90° , and every other 90° they switch to the next one. In partial analogy to what happens to Earth, seasons are divided into three months each, for a total of 12 months. These months are simply called with a number from 1 to 12, and everyone lasts precisely for 30° of solar longitude.

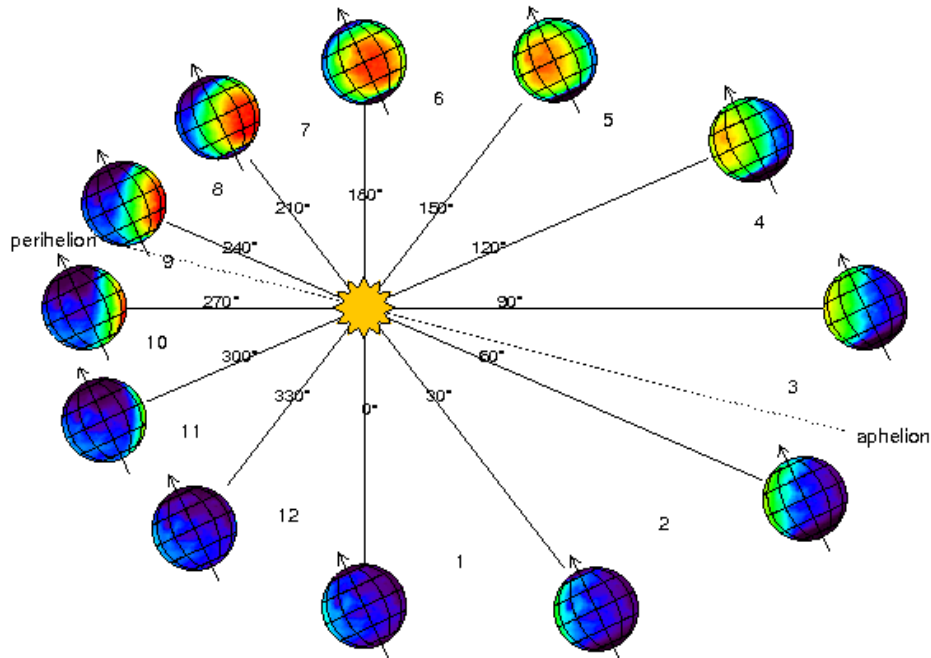


Figure 19: Martian solar longitude representation [27].

In addition to the aforementioned components the planet's atmosphere is always dusty, and dust storms can be frequently seen on several scales [25]. Figure 20 shows the registered high variability of the dust cycle during the year in terms of opacity in the $9 \mu\text{m}$ wavelength.

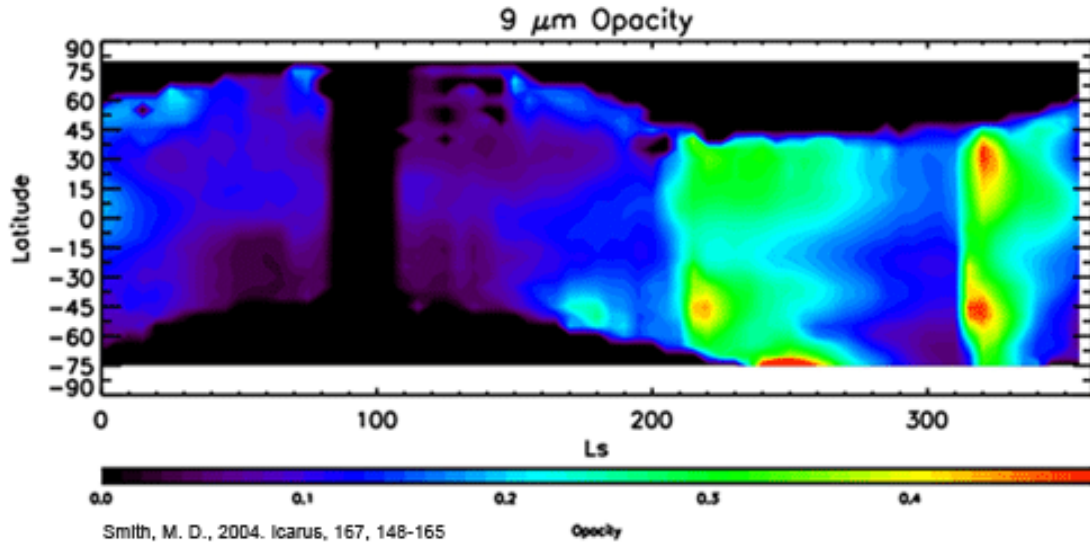


Figure 20: Dust annual cycle on Mars expressed in opacity in the $9 \mu\text{m}$ wavelength in function of latitude and solar longitude.

Cloud hazes and water frost are frequent as well, and even CO_2 , during the respective winter, condensates in one of the two poles. Polar caps made of a combination of H_2O and CO_2 surface ice (with strong dust contamination) are therefore visible during winters, autumns and spring, but they almost disappear during summer season and sometimes during early (late) autumn (spring) as well.

2.3 The Instrument

This imaging spectrometer is capable of covering wavelengths between 0.362 and 3.92 μm at 6.55 nm/channel [28].

It consists mainly of three distinct parts: the Optical Sensor Unit (OSU), the Gimbal Motor Electronics (GME) and the Data Processing Unit (DPU) (Figure 21).

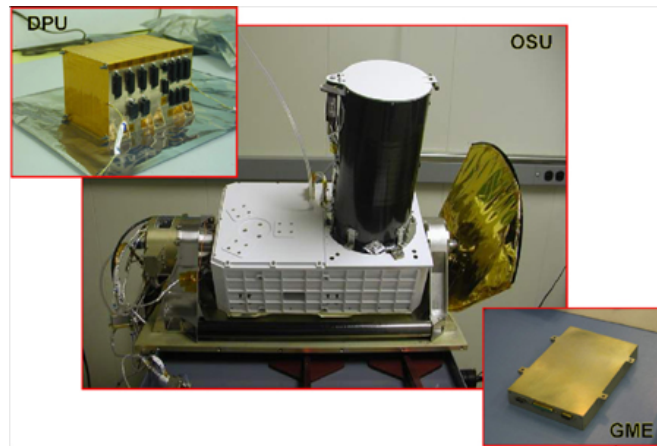


Figure 21: CRISM instrument components [28].

The **Optical Sensor Unit** contains a Ritchey-Chretien telescope with a 2.06° field of view (FOV) that focuses the light on the entrance slit of the dual spectrometer [31].

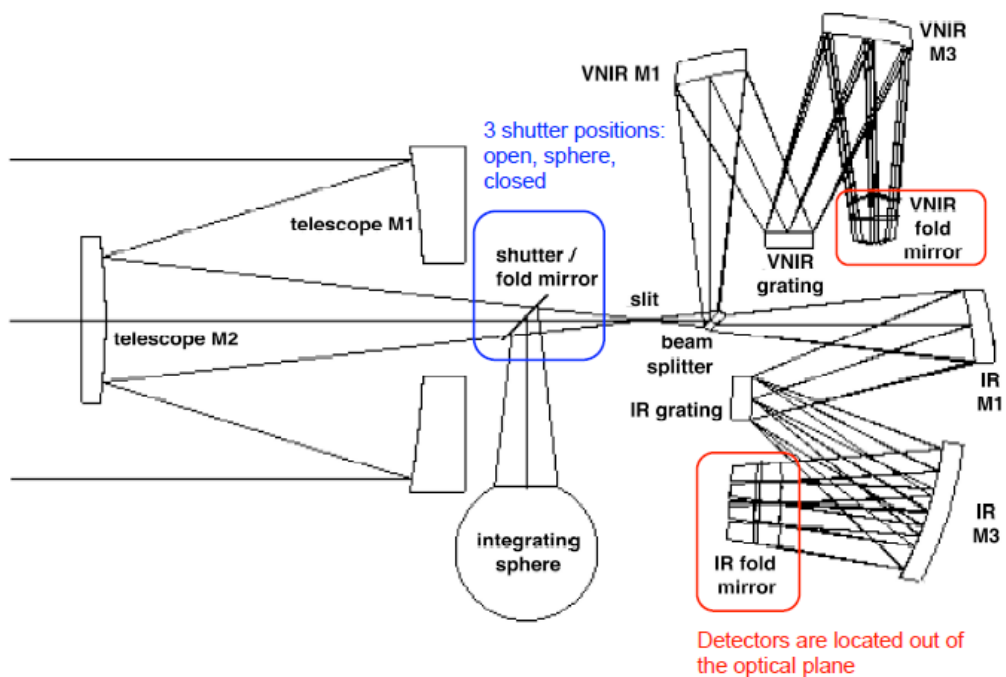


Figure 22: CRISM optics representation [30].

In figure 22 one can see the CRISM optical design. On the leftmost side there is the Ritchey-Chretien telescope, which is a variant of the Cassegrain telescope that has a hyperbolic primary mirror and a hyperbolic secondary mirror, and it's useful to eliminate off-axis aberrations. After the M2 mirror the light passes through a shutter, which can be closed, open or can let only the light from the integrating sphere to pass (calibration measurements). After passing through the slit the radiation is split by a dichroic into VIS-NIR and IR beams. The spectral image of the slit is then focused onto a two dimensional focal plane (FP) and continuously sampled with 6.55 nm spectral spacing and an Instantaneous Field of View (IFOV) of 60 μ radians.

The VIS-NIR detector has 107 illuminated rows, while the IR detector has 438 useful rows. By combining all of them, the spectrometer has a total of 545 channels in the spectral direction, with 640 pixels per row.

In addition to this part in the unit there are also a gimbal to remove smear due to spacecraft motion, cryocoolers for the infrared detectors, radiators to keep all the instrument cold, and electronics.

The **Gimbal Motor Electronics**, instead, is responsible for commanding and powering the gimbal, and at the same time it "analyzes data from its angular position encoder in a feedback loop" [28].

Finally, the **Data Processing Unit** acts as a link between the spacecraft and the commands from the OSU.

2.3.1 Observations

For each observation it is possible to select only a portion of these rows, and it's even possible to group the pixels corresponding to the same row with a 2x, 5x or 10x pixel binning [32, 33].

Depending on the requirements the instrument can either constantly point in the nadir direction or progressively changing its orientation to track a specific point on the surface. With row selection one can take both hyperspectral observations, where all the rows are used to get the spectrum for each pixel, or multispectral observations, where instead only 63 to 93 channels are used to get images at a specific wavelength range.

Usually dynamical pointing involves hyperspectral observations. This kind of observation is based on retrieving the same image along a continuous spectral band. In the case of CRISM, hyperspectral imaging can vary with the pixel binning along the following cases [31, 32, 33]:

- Full Resolution Targeted (FRT), with no binning and a spatial resolution of 18 m/pixel
- Half Resolution Short (HRS), with 2x binning and resolution of 36 m/pixel
- Half Resolution Long (HRL), with the same characteristics of HRS, but with a swath width twice as long
- Hyperspectral Survey (HSP), with 10x binning and resolution of 200 m/pixel. These are nadir measurements, specifically aimed at the observation of the polar caps

Multispectral observations retrieve instead images along a discrete distribution of spectral bands, and in this case are divided into [33]:

- Multispectral Survey (MSP), with 10x spatial binning, a resolution of 200 m/pixel and designed to accomplish coverage rapidly
- Multispectral Window (MSW), with 5x spatial binning, a resolution of about 100 m/pixel and capable to have a high resolving power in key areas

Targeted observations do not cover the whole planet, while nadir ones allow for an almost global coverage of Mars [33].

The data specifically used in this project have been retrieved from the Planetary Data System (PDS), and are mainly included in these categories:

- Targeted Reduced Data Record (TRDR, with extension `.trr3`). They include both targeted and nadir observations (expressed in units of I/F), which are already corrected for atmospheric, photometric and thermal effects
- Map-projected TRDR (MTRDR, with extension `.mtr3`). These files combine several targeted hyperspectral observations into single map tiles

In parallel to these two data types, Derived Data Records (DDRs, with extension `.ddr1`) containing information regarding the geometry of the observations, and the surface temperature are retrieved. Each of these files on the PDS is accompanied by its corresponding label file (with extension `.lbl`).

2.4 Surface Ice Detection

The method adopted in this research consists in using spectral indices in the VIS-NIR band and associate them to the radiance values measured, also referred to as I/F, measured by CRISM at different wavelengths via the following equation:

$$I/F = \frac{L_{MARS}}{E_{EARTH}d_{AU}^2} \quad (11)$$

Where L_{MARS} is the spectral radiance of Mars, E_{EARTH} is the spectral irradiance of the Sun at Earth's location, and d_{AU} the distance between the Sun and Mars in AU.

The spectral indices are a measure of the depth of the absorption band of the considered species and are usually defined with the help of model spectra. An example of the use of model spectra is a study led by the Institut d'Astrophysique Spatiale (IAS) team for the OMEGA instrument. This is a VIS-NIR/SWIR spectrometer that was designed to characterize the Martian surface composition and to study the "spatial and temporal distribution of CO₂, CO, H₂O and aerosols (dust particles) in the atmosphere" [34]. This team is the same leading group that is working on MAJIS at IAS. In this study, simulated spectra for H₂O and CO₂ ices with different grain sizes were compared [35]. Figure 23 shows the results of this study in terms of reflectance in function of the wavelength for different CO₂ (orange and red) and H₂O (green and blue) ice grain sizes.

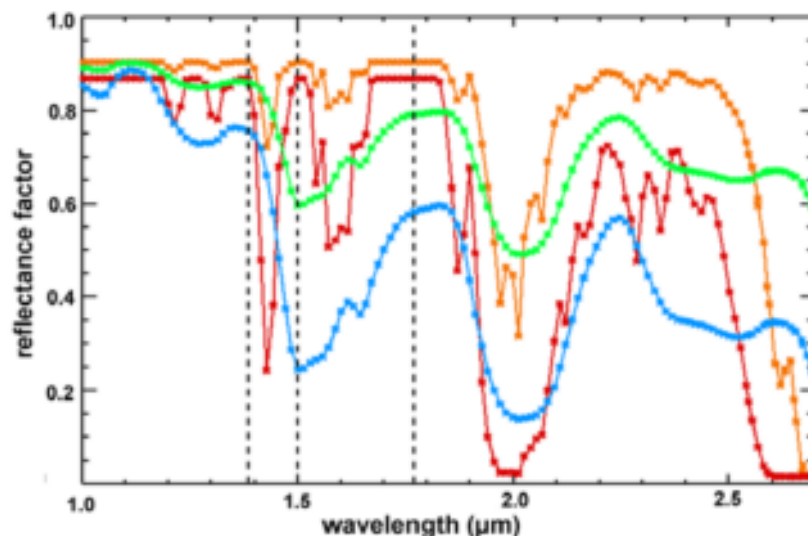


Figure 23: Simulated spectra from the IAS study [35] for different grain sizes. In orange (1 mm) and red (5 cm) there are the CO₂ surface ice simulations, while in green (10 mm) and blue (100 mm) the ones for H₂O ice.

A comprehensive list of spectral indices defined for CRISM datasets has been compiled by Pelkey et al.[36]. This list was updated recently by Viviano-Beck [37]. CRISM spectral summary files, available on the PDS, store by default the values of the indices for some MTRDR images. They are useful for the detection of several surface components like H₂O ice, CO₂ ice, silicates, mafic, ferric and hydrate minerals. The majority of the indices there defined are derived by selecting three characteristic wavelengths for a given absorption band [37], all of them with their corresponding I/F:

- A shorter wavelength λ_S (R_S factor) that is a part of the continuum to the left of the absorption band
- A central wavelength λ_C (R_C) as the minimum of the absorption band
- A longer wavelength λ_L (R_L) being a part of the continuum to the right of the absorption band

The depth of the absorption band comes from the linear interpolation of R_S and R_L , the evaluation of the interpolant at λ_C , and finally the comparison of R_C with its interpolated value R_{C*} :

$$R_{C*} = aR_S + bR_L \quad (12)$$

where

$$b = \frac{\lambda_C - \lambda_S}{\lambda_L + \lambda_S} \quad (13)$$

and

$$a = 1 - b \quad (14)$$

Finally the depth at λ_C is found in the following way:

$$BD(\lambda_C) = 1 - \frac{R_C}{R_{C*}} = 1 - \frac{R_C}{aR_S + bR_L} \quad (15)$$

The spectral indices for surface ice detection are shown in Table 1.

Index	λ_S [nm]	λ_C [nm]	λ_L [nm]	Compound
BD1500	1367	1525	1808	H ₂ O ice
BD3100	3000	3120	3250	H ₂ O ice
BD1435	1370	1432	1470	CO ₂ ice
BD3200	3250	3320	3390	CO ₂ ice

Table 1: Spectral parameters for the detection of surface ice. The first twos are for H₂O ice, while the others are for CO₂ ice [37].

Among the ones showed in the table, the most used Band Depths (BDs) are the ones at 1500 nm and 1435 nm because of the presence of a local maximum for the Signal to Noise Ratio (SNR) at 1500 nm. Furthermore the detector saturates for optical path lengths higher than the maximum detectable for other absorption bands and the band at 1435 nm (CO₂) is very narrow, being therefore less affected by H₂O ice presence.

The indices taken as a reference were specifically developed for the CRISM spectrometer. They are BD1500 and BD1435 because of the aforementioned reasons. Each index that has been defined is then compared to its respective reference one taken from table 1.

The index to be tested and the reference one are mapped on the same CRISM MTRDR image tile. From the work of a previous student, five scenes were chosen for the index validation process, with different surface compositions and variability, both from one scene to the other and within a same scene.

The chosen CRISM observations for index validation are the following.

- FRT0000783D (80S, 20E): H₂O ice + CO₂ ice + ice-free surface
- FRT00002f7F (85N, 20E): H₂O ice + ice-free surface
- HRL0000815A (84S, 7E): H₂O ice + CO₂ ice + ice-free surface
- HRL0000ADCC (78N, 27E): H₂O ice + ice-free surface
- FRT00006825 (78S, 10E): CO₂ ice

2.5 Baseline Software

The CRISM images can be processed using MATLAB scripts written specifically for this project.

The first version of the software was already available from the work of a former intern at ROB, while a second intern updated it to v2 and v3. The core functions allow the user to:

- Read and store CRISM .mtr3, .trr3 and .ddr1 files.
- Map an index over a single image file.
- Display the index values in a latitude - longitude or pixel - pixel plot.

The code had been tested only for few specific locations and it was written with the sole purpose of reading specific CRISM images. The values of the parameters that in the successive versions were read directly from the labels associated with each file were therefore hard-coded. and there was the need for it to be capable of analyze the temporal evolution of the whole polar cap. For all the three versions of the software already in possession of ROB the problem was that they weren't optimized to analyze the high amount of data required for the study of the temporal evolution of the polar cap.

One of the objectives of the ROB team was therefore to improve the software to make it capable of processing this huge amount of data.

2.5.1 CRISM Software v2

The first improvement in this version is simply a function that reads the label files associated with each file. The label is a text file which gives important information about the image file it refers to, and it's extremely helpful to retrieve automatically information from the data files.

In particular, the parameters which are usually read from the label files are the number of pixel rows in the image (L), the number of pixels columns (H), the number of spectral channels (NC, i.e. the number of wavelengths sampled by each pixel), and the areocentric solar longitude at the time of the observation.

The label file contains even the name of the image file it is related to, as well as the names of the derived files. Among them the most important derived file is the DDR, which, as previously stated, includes the observation geometry.

The values of elements of the sampled wavelength vector with the same position index are not constant along the pixels of a same row, while they are constant along a column. This is due to a common effect happening in pushbroom sensors like CRISM, which is called **Spectral Smile**, that makes the spectral response non-homogeneous along the across-track position [38]. To compensate for this phenomenon only one of those matrix column vectors has been chosen as the wavelength vector to be used in the subsequent computations. More into detail, the wavelength corresponding to the central pixel of the row. This choice has been done because, as noticeable in the CRISM laboratory studies (Figure 24), the smiling is more prominent at the rows' edges. Another reason why this method was adopted is that the wavelength shift along a row doesn't go beyond 1 or 2 nm, which is below half the spectral resolution of CRISM (around 7 nm). This means that it's safe to assume that a sampling of the I/F at a wrong wavelength point is nearly impossible.

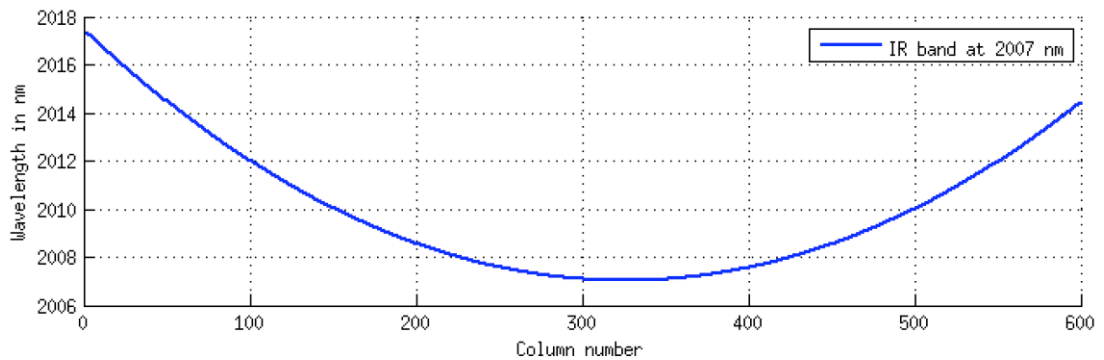


Figure 24: Smile effect on a CRISM IR image [38].

Another way to correct these distortions is to average the value of each I/F used in the index over five wavelength point, with the nominal one at the center [37]. This option has not been eventually implemented because it is very demanding in terms of processing power and the provided corrections proved to be quite negligible.

To further improve the processing capabilities of the software, in the new version of the software, for a desired wavelength the closest element in the wavelength vector and its respective spectral index are retrieved, instead of working with only one index at a time because of hard-coded values, like in the case of the first version. An image cube is then evaluated at the retrieved index in the spectral direction, yielding the matrix of the I/F at the selected wavelength. Matrices corresponding to the various chosen wavelengths are then combined according to Equation 15 into a new matrix containing the values of the indices over all the image pixels. In this regard, the improvement in the processing speed comes from

the substitution of loops with matrix operations.

Image cubes can be very demanding in terms of memory storage (around 300 MB for a .trr3 file and 1GB for a .mtr3 file), so processing more than one file at the same time can easily lead the machine to run out of memory. Luckily for a big part of the data analysis the full mapping of the whole image is not needed, and only a localized set of indices is needed. Because of that, a new function capable of reading and storing information for a single pixel (with its position as the input) is present.

2.5.2 CRISM Software v3

A binning in latitude and longitude for the values of the indices and small procedural changes to improve processing speed have been added in this version.

The problem with all the versions of this software was that, despite its efficiency in loading and processing the huge amount of data from CRISM observations, the code was not yet optimized for large data analysis, as required by the study of the temporal evolution of the polar caps. Indeed, if one had used it for a specific set of solar longitudes (L_s), besides the plotting the pixels he wouldn't have been able to both map accurately the polar cap and understand its temporal evolution.

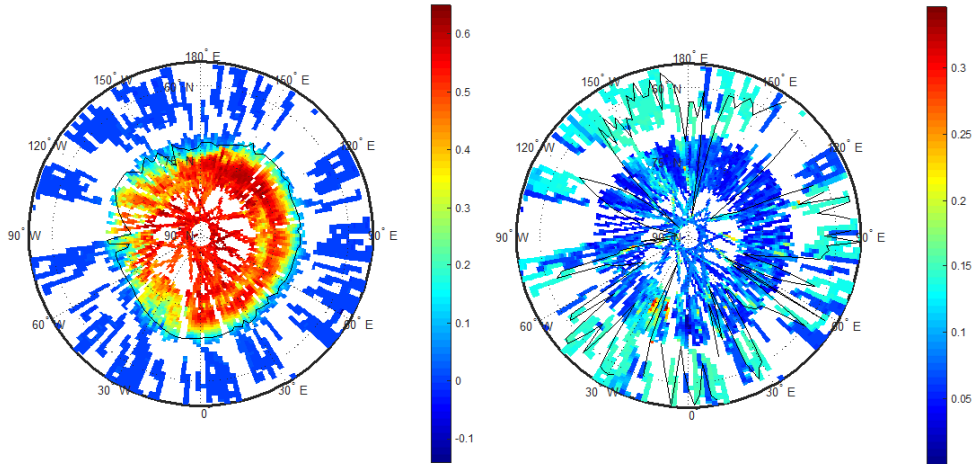


Figure 25: CRISM_v3 North pole pixel plot and ice caps mapping for MY = 29 and L_s between 57° and 64° (spring time). On the left: surface H_2O ice. On the right: surface CO_2 ice. The black lines represent the (noisy) polar caps borders. The "spaghetti strand" appearance, like it was defined in Brown et al. [23], is due to a swath width on ground of ~ 10 km.

In Figure 25 the indices are applied on each surface location. The left plot represent surface H_2O ice, while the one the right the surface CO_2 ice. Colourless pixels correspond to areas where no signal has been detected. The colour warmth of the pixels represent the different values of the considered indices. The black line

represents what is computed to be the shape of the ice cap. Despite the plot on the left might suggest that the software incorporates a correct method to properly map the surface ices, some unwanted noise is already detectable and the plot for the CO₂ shows that a method to reduce the noise needs to be implemented to properly detect the edges of the polar cap.

Furthermore, a more in depth analysis done with multiple L_s ranges showed that a high amount of noise can rise even for the H₂O ice.

The code is even capable to save all the analyzed data relative to the edges of the caps to later plot all the considered L_s ranges in one single latitude-longitude plot.

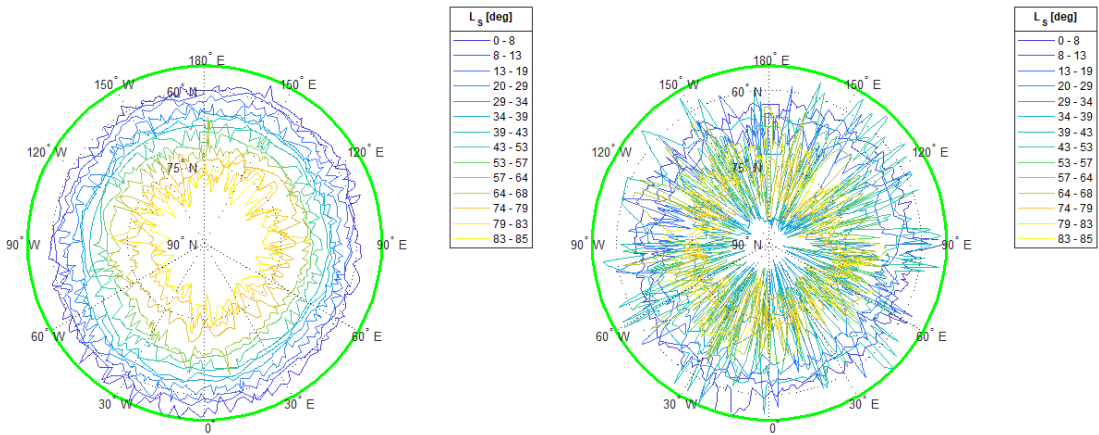


Figure 26: CRISM_v3 North pole ice caps mapping for MY = 29 and multiple solar longitudes for the spring time. On the left: surface H₂O ice. On the right: surface CO₂ ice. The black lines represent the (noisy) polar caps borders. The latitude limit for the plots is set at 55°N.

Figure 26 shows indeed that no proper qualitative consideration can be applied from the CO₂ data processing, while, despite an inverse growth trend can be assumed for surface H₂O ice, its analysis still shows an intolerable amount of noise.

A reference edge detection comes from Brown et al. [23] and Piqueux et al. [39], who both show, respectively in Figure 27 and Figure 28, polar edges after noise reduction processes. As noticeable from these plots, despite for some specific L_s the water ice cap might have a tolerable amount of noise, for the totality of the CO₂ ice edges and for $L_s > 50^\circ$ for water the noise needs to be reduced.

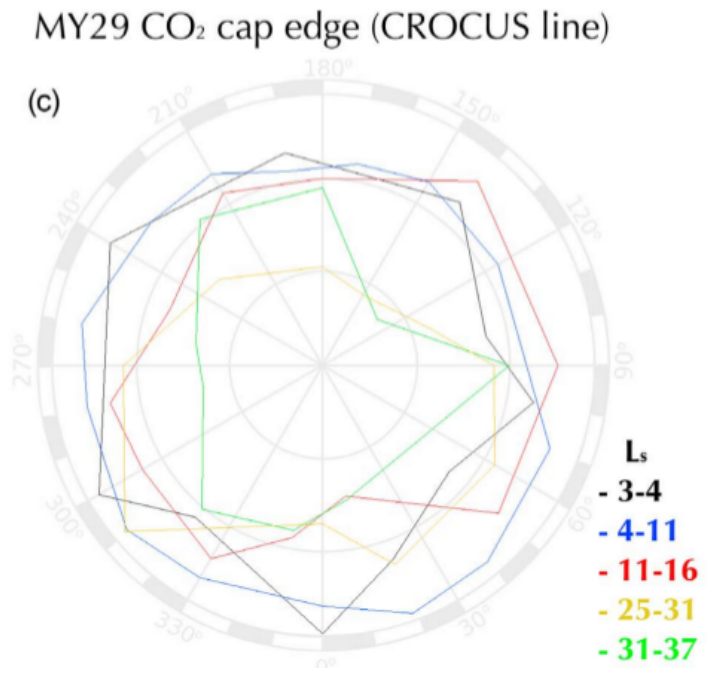


Figure 27: CO₂ polar cap temporal evolution for MY 29. From Brown et al. [23]

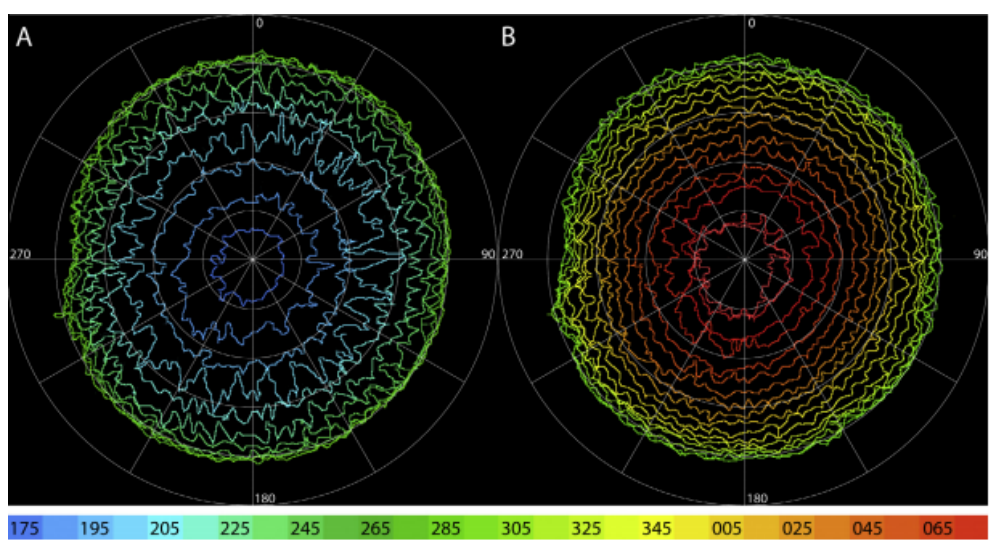


Figure 28: CO₂ polar cap temporal evolution for MY 30-31. From Piqueux et al. [39]

2.6 CRISM Software v4 Development

Considering the potentiality of the software, the ROB team needed, in order to retrieve the evolution of the polar caps, to optimize the software to make it capable of handling large amounts of data. In this regard the main focus in the development of version 4 has been to reduce the noise to properly detect the polar edges.

2.6.1 Scripts Improvement

In this frame the first goal was to improve the **automation** of the whole script. The code was indeed made more user friendly and more efficient in handling large dataset. In this case, the considered dataset for the Martian spring of MY 29 was worth around 1 TB and its total processing time, considering the data for both H₂O and CO₂ approximately amounts to a full day of work. The code was then modified in order to be operable by the simple specifications in the input folder, the output folder, and whether the processed data were for H₂O or CO₂ surface ice (by the change of a single numerical input).

The second point, closely related to the first one, was to improve **operability** and **comprehensibility** for the users. This means that whoever will operate the scripts in the future can now better comprehend the logic behind the scripts and therefore customize them, if needed. A new editing session has been done in order to clean, compact and explain everything written in the code.

These improvements so far, led to an increase in automation in the software and therefore saved a good amount of space.

A final correction in the code, regarding the reduction of visualized data during the analysis process, led the average run time for a single solar longitude range to pass from 17 to 15 minutes, with therefore a average increase in the **processing speed** around 11%.

2.6.2 Data Analysis

First of all, in order to gain a qualitative estimation of the surface ice size and temporal evolution, a solution for the noise noticed from the comparison between the software's output in Figure 26 and the works of Brown et al. [23] and Piqueux et al. [39] had to be found.

Two different solutions were proposed:

- **Data binning** for equally spaced ranges of latitudes, combined with an averaging process.
- **Moving mean** along the whole set of longitudes.

Both of them were applied to all the dataset by rerunning all the software pixel by pixel. Then the resulting edges coordinates were in the first case binned in equally spaced longitude ranges and their latitudes were averaged, while in the second case, instead, each retrieved latitude of the polar edge was substituted with the average value of the first n latitude values longitudinally closer it. In these circumstances, the former method gives, as noticeable in Figure 29 where the outputs of the two different values are represented in a latitude-longitude plot, a more circle-like shape to the surface ice. This would be from one side a very simplistic representation of the real shape of the analyzed surface ice, but on the other hand it would be a very simple way to standardize shapes and therefore to obtain a clear qualitative representation of the surface area for temporal comparisons. The latter, instead, lacks the circular simplicity for areas comparison and therefore there's a higher risk for the shapes at different solar longitudes to overlap, but nevertheless it describes with much more accuracy the shape of the polar cap. Both options were implemented in the scripts, so future users will be able to easily switch between the two methods with the simple change of an input variable.

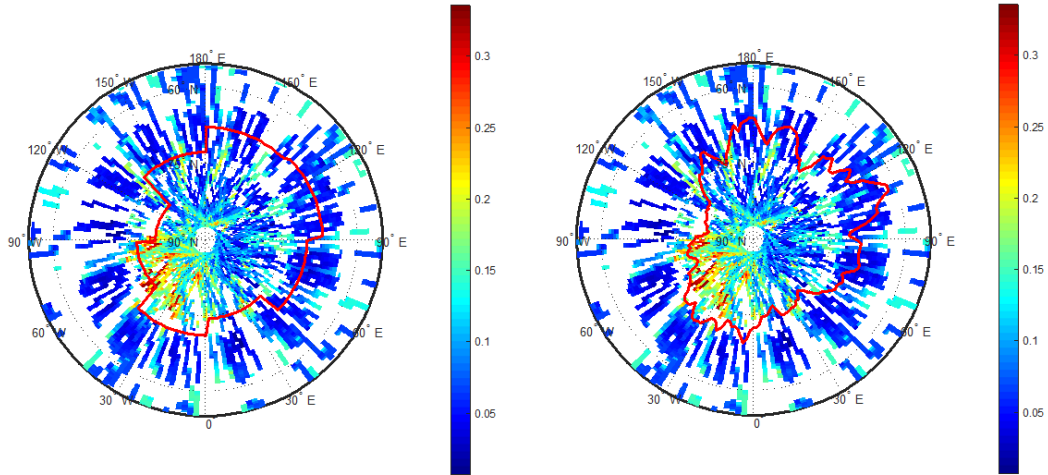


Figure 29: CRISM_v4 Plots for the CO₂ surface ice at $L_s = 34^\circ - 39^\circ$. On the left: the 45° latitude-binning method. On the right: moving mean.

The binning range has been chosen at 45° because shorter ranges would have led to a higher variability of the averaged latitudes without adding any new information that couldn't already be retrieved with the application of the moving mean.

The dataset range for the moving mean was set for H₂O and CO₂ ice at respectively 11 and 19 values longitudinally both before and after the considered central element. These specific ranges were chosen for two reasons: first of all an odd number is by definition required to have the sample window centered on the point of interest. Secondly, different sample windows were tested and it was found that lower values would have generated noisier profiles, while higher values would have led to an oversimplification of the shape of the polar cap.

The moving mean was eventually chosen for this task, because a quantitative analysis of the extension of the polar cap was already planned, and therefore the data binning method, being mostly useful a qualitative representation of the extension of the polar cap rather than its shape, would have been almost redundant. In a second instance, a **Cartesian representation** of the polar caps coordinates has been implemented to have a better qualitative surface representation than the meridian plots.

As previously mentioned, to have a clearer idea of the time variations in the north pole, a **quantitative representation** of the total extension of the polar caps has been implemented. The area in this case has been calculated from a spherical approximation, with a radius equal to the planet's polar radius (3376.2 km, from NASA database).

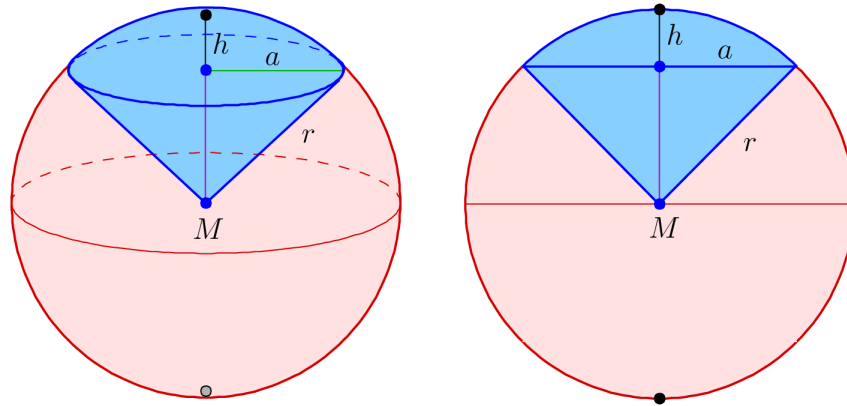


Figure 30: Geometry of a sphere. Image from Wikipedia.

Like it's obvious from Figure 30, a simple trigonometric calculation is enough to convert the values of latitude and longitude in kilometers. After this calculation was implemented in the code, the trapezoidal method has been included to finally compute the ice caps areas.

Finally, a code for loading data from models and qualitatively compare them with the results from the spectroscopic analysis has been applied. This part can be efficiently used to compare resolutions or, in case a $\frac{kg}{m^2}$ map is inserted as a comparison, it can help to give an idea of the resolution capacities of the considered spectrometer.

2.7 CRISM Analysis Results

In order to both train the software with real measurements and study the climate of Mars, the actual CRISM spectroscopic data for the Martian north pole was analyzed. The data at the team disposal, because of data storage and band speed requirements, is only relative to the spring of MY 29. This year corresponds to a period on Earth between 09/12/2007 and 26/10/2009. This period was chosen because it would have had (in theory) visible CO₂ surface ice, and because a comparison with the literature would have been possible, since Brown et al. [23] chose the same period for his study.

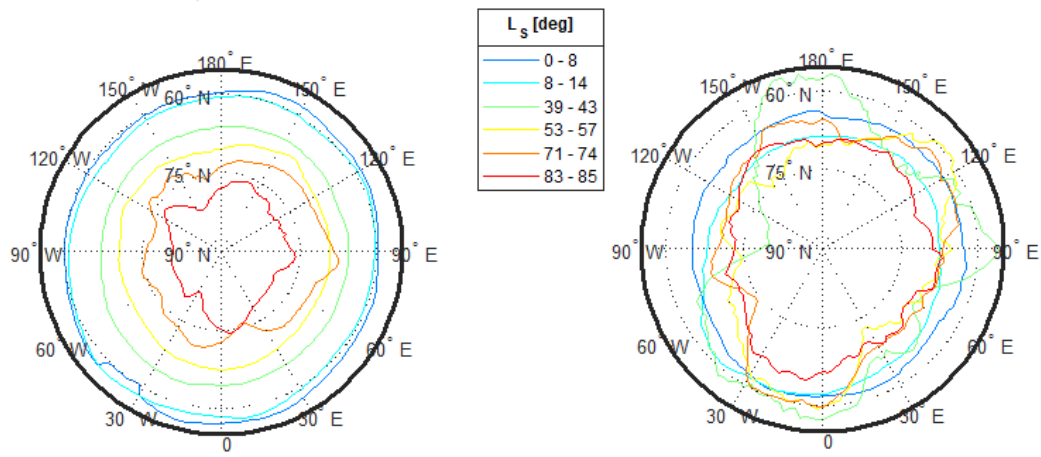


Figure 31: Ice caps temporal evolution for MY 29 expressed as geographical position in function of solar longitude. On the left: H₂O surface ice. On the right: CO₂ surface ice.

Figure 31 shows the temporal evolution of the north pole for certain ranges of solar longitude. To make the plot easy to understand, some temporal ranges along the Martian spring were suppressed. The reader can find an almost continuous set of solar longitudes in Figure 32.

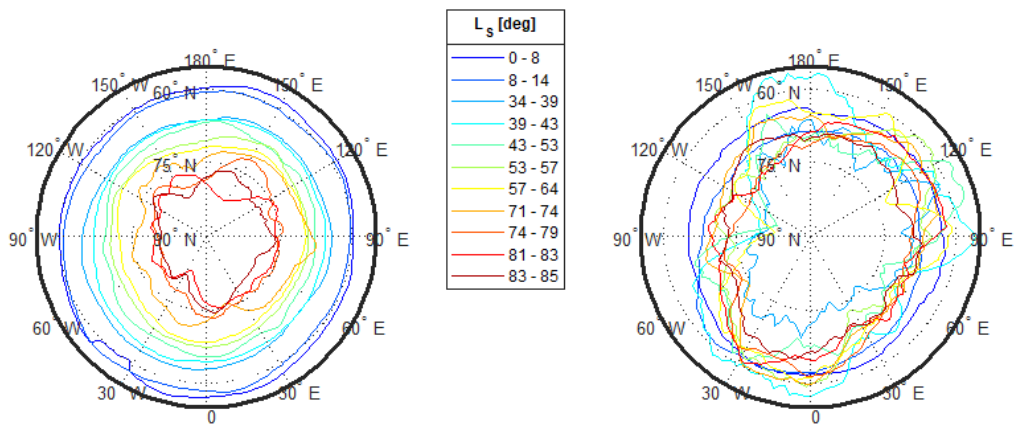


Figure 32: Ice caps temporal evolution for MY 29 expressed as geographical position in function of a full set of solar longitudes. On the left: H₂O surface ice. On the right: CO₂ surface ice.

As already visible from Figure 31, there seems to be a lower trend of decrease in the CO₂ ice rather than in the water ice. This is even confirmed by Figure 33, where qualitative estimation of the sizes of the polar ice caps are plotted in function of the considered L_s ranges. Here an even higher abundance of CO₂ surface ice than the one of water ice for $L_s > 74^\circ$ is noticeable.

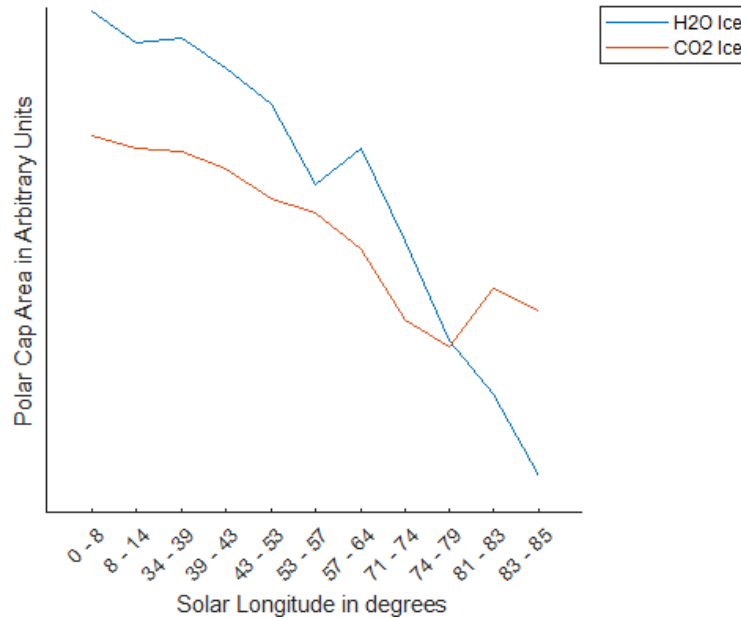


Figure 33: Ice caps temporal evolution for both H₂O and CO₂. Data from the Martian spring of MY 29. [Not in scale].

These results are far from being enough to suggest that the northern CO₂ ice cap in late spring either recovers or is extremely more extended than the water ice one. Considering the uncertainties for the indices and the risk of contamination of surface ices during warmer periods, there might be the possibility to have received false signals from that time range. Another possibility is that this increase might be caused by the detection of CO₂ frost on other solid surfaces, which is processed in the analysis as surface ice. It's nevertheless important to notice that this behaviour is unlikely to be attributable to an outlier, considering that more than one solar longitude range was noticed to have this unexpected increase of the CO₂ ice cap. The variability of the polar cap edges, calculated via the standard deviation of the data in the same longitude range used for the moving mean/binning process, is comparable with the thickness of the plotted line in figure 33, and therefore cannot be the cause of this unexpected behaviour. This unexpected result might therefore be a base to start from for future researches and reanalyses.

The literature comparison shows a correspondence in shapes for the polar caps in MY 29 for comparable solar longitude ranges. Additionally, with the method previously mentioned, an angular resolution around one order of magnitude higher than the one from Brown et al. [23] (Figure 27) has been retrieved. On the other side, though, different extensions for the CO₂ polar cap for the same martian year can easily be noticed from the comparison with this study. This might be caused by the previously mentioned divergence in spatial resolution. Unfortunately, no one has yet analyzed the CO₂ polar cap at solar longitudes higher than 40° for MY 29 before, so no study comparison can be used for the unusual trend detected in Figure 33 for $L_s \geq 74^\circ$.

A possible starting point for future studies might be comparing the retrieved data and trends with both different imaging instruments and CRISM analysis for spring periods in different martian years.

This work, in addition to the one of the whole ROB team led by Dr. Karatekin, gave enough scientific data to present a poster at the EPSC-DPS Joint Meeting 2019 in Geneva, Switzerland, entitled [24]:

EPSC-DPS2019-1804

Evolution of Mars polar caps extent from CRISM data
by Alfonso Caldiero et al.

In session TP1 – Mars Interior and Surface

3 Conclusions

For the **MAJIS VIS-NIR characterization mission**, from the scripts provided by the ROB DeMeLab-STCL team, a software package in Python, capable of processing input images to retrieve the required parameters for the characterization, has been delivered. The software's output images are corrected for the fixed pattern noise and the perturbation measured in the reference columns. The successful implementation of this method has been confirmed by close-to-zero signal in the reference columns of the processed input Teledyne dark images and from the comparison with the CDS images processed by the IAS team.

Additionally, a detection model, capable of simulating measurements in light and dark conditions, has been updated and modified to give the team the opportunity of having proper simulated images for software training purposes. This model's outputs were used to validate and train the developed software. The validity and the proper functioning of the whole software has been confirmed from the simulated data.

A software user guide was finally given to the team to show the future operators how to successfully use the packages, and in case to solve most of the common problems that they might have.

For the **CRISM Martian North Pole analysis**, instead, the previously developed MATLAB data processing software has been updated and improved, and a full data analysis software, capable of retrieving both shape and size of polar CO₂ and H₂O surface ice caps, has been delivered.

Most of the results from the analysis of the Martian spring in MY 29 are in agreement with both theory and literature in terms of noise levels and polar caps shapes, even with a probable improvement of the angular resolution. An unexpected behaviour of CO₂ surface ice has been noticed for solar longitudes superior to 74°. Furthermore, the extension of the computed CO₂ polar cap has been noticed to be higher the one registered in Brown et al. [23], probably due to the different angular resolutions. These results will be of interest for future studies, in terms of both reanalysis of the same data set and comparison with other Martian years or different instruments.

With these results at hand, and considering that the software has been already tested with real spectroscopic images, its potential future use for the data retrieved from the Jovian moons by the JUICE-MAJIS mission, after an ad-hoc adaptation work, is considered feasible.

References

- [1] ESA JUICE website,
<http://sci.esa.int/juice/>
- [2] "Arianespace and ESA announce Jupiter Icy Moons Explorer launch contract",
<http://sci.esa.int/juice/61415-arianespace-and-esa-announce-jupiter-icy-moons-explorer-launch-contract/>
- [3] BIRA-IASB MAJIS website,
<http://planetary.aeronomie.be/en/majis.htm>
- [4] MAJIS science and technical team, *JUICE - JUpiter Icy Moons Explorer MAJIS - Moons And Jupiter Imaging Spectrometer Experiment Interface Document - Part B*. 2014.
- [5] G. Piccioni et al., *MAJIS (Moons And Jupiter Imaging Spectrometer) for JUICE: Jupiter system objectives*. EPSC, 2013.
- [6] Y. Langevin et al., *The MAJIS VIS-NIR Imaging Spectrometer for the JUICE Mission*. EPSC, 2014.
- [7] Czerny-Turner configuration,
https://en.wikipedia.org/wiki/Monochromator#Czerny%E2%80%9393Turner_monochromator
- [8] Leonardo Tommasi et al., *The Advanced Optical and Thermomechanical Design of the JUICE/MAJIS Spectrometer*. 2018.
- [9] Teledyne Technologies Inc.,
https://en.wikipedia.org/wiki/Teledyne_Technologies
- [10] Paul Jerram and James Beletic, *Teledyne's high performance infrared detectors for space missions*.
ICSO October 2018
- [11] J. W. Beletic et al., *Teledyne Imaging Sensors: Infrared imaging technologies for Astronomy & Civil Space*.
SPIE Vol. 7021, from 70210H-1 to 70210H-14
- [12] Miriam E. Cisneros-González et al., *Design of the calibration bench for the characterization of MAJIS/JUICE VIS-NIR detectors*. EPSC, 2018.
- [13] Miriam E. Cisneros-González et al., *Validation tests of the calibration bench for the characterization of MAJIS/JUICE VIS-NIR detectors*. EPSC, 2019.
- [14] Integrating Sphere,
https://en.wikipedia.org/wiki/Integrating_sphere

- [15] Lionel Van Laeken, *Development of experimental benches for radiometric characterization Application to space instrument MAJIS VIS-NIR on JUICE*. Page 20. 2019.
- [16] Miriam E. Cisneros-González et David Bolsée, *VIS-NIR Detectors Characterization Procedure*. BIRAIASB Internal Document*.
- [17] David Gardner, *Characterizing Digital Cameras with the Photon Transfer Curve*.
- [18] *Electro-Optical Test Methods for Charge Coupled Devices*. European Machine Vision Association
- [19] *WFC3 Data Handbook*. Section 6.5, 2010
- [20] *Electro-Optical Test Methods for Charge Coupled Devices*. ESCC Basic Specification No. 25000
- [21] Short wave pass filter description (Lambda Inc.),
<https://www.lambda.cc/product/long-short-wave-pass-filters-lwp-swp/>
- [22] Short wave pass filter description (Evaporated Coating Inc.),
<https://www.evaporatedcoatings.com/long-wave-pass-short-wave-pass-optical-filters/>
- [23] Adrian J. Brown et al., *Compact Reconnaissance Imaging Spectrometer for Mars (CRISM) north polar springtime recession mapping: First 3 Mars years of observations*. 2012.
- [24] Alfonso Caldiero, Özgür Karatekin, Orkun Temel and Amedeo Romagnolo, *Evolution of Mars polar caps extent from CRISM data*. EPSC, 2019.
- [25] J. W. Chamberlain & D. M. Hunten, *Theory of Planetary Atmospheres*.
- [26] Timekeeping on Mars,
https://en.wikipedia.org/wiki/Timekeeping_on_Mars
- [27] Mars Climate Database,
http://www-mars.lmd.jussieu.fr/mars/time/solar_longitude.html
- [28] CRISM website,
<http://crism.jhuapl.edu/index.php>
- [29] NASA CRISM website,
https://www.nasa.gov/mission_pages/MRO/spacecraft/sc-instru-crism.html
- [30] Scott L. Murchie et al.,
CRISM Instrument, Mission, and Data Set Description. 2009

- [31] Peter R. Silverglate, Dennis E. Fort,
System design of the CRISM (compact reconnaissance imaging spectrometer for Mars) hyperspectral imager. Proc. SPIE 5159, Imaging Spectrometry IX, (7 January 2004)
- [32] Scott Murchie et al.,
CRISM Data Product Software Interface Specification. 2006
- [33] Scott L. Murchie et al.,
CRISM data product software interface specification. Version 1.3.7, 2012
- [34] OMEGA website,
<https://mars-express.cnes.fr/en/MEX/omega.htm>
- [35] Y Langevin et al.,
Observations of the south seasonal cap of Mars during recession in 2004–2006 by the OMEGA visible/near-infrared imaging spectrometer on board Mars Express. Journal of Geophysical Research: Planets, 112(E8), 2007.
- [36] SM Pelkey et al.,
CRISM multispectral summary products: Parameterizing mineral diversity on Mars from reflectance. Journal of Geophysical Research: Planets, 112(E8), 2007.
- [37] Christina E. Viviano-Beck et al.,
Revised CRISM spectral parameters and summary products based on the currently detected mineral diversity on Mars. Journal of Geophysical Research: Planets, 119(6):1403–1431, 2014.
- [38] Xavier Ceamanos and Sylvain Douté,
Spectral smile correction in CRISM hyperspectral images. Laboratoire de Planétologie de Grenoble, 2009.
- [39] Sylvain Piqueux et al.,
Variability of the martian seasonal CO₂ cap extent over eight Mars Years.

*To access the internal documents or have further information, the reader should contact the BIRA team and formally ask for a partial access to the documentation.

Acknowledgments

I'm sorry that I will not be able to thank one by one all the people that made my life an amazing adventure, but unfortunately I cannot write a novel-sized acknowledgement section in my thesis, so I will just say that in this amazing moment of my life, my mind is going back to all the events and all the people that are part of my personal story. So, if you ever happened to cross my path, dear reader, be sure that this acknowledgement is even dedicated to you.

First and foremost I would like to thank the University of Liège for the wonderful experience that has given to me during these last two years, and in particular Professor De Becker, who patiently helped a student with serious problems with bureaucracy and deadlines to arrive at the end of this amazing master degree. Similarly, a special thanks goes to the Royal Observatory of Belgium, the Royal Institute of Aeronomy, all the MAJIS team and Dr. Dehant for the great internship I had the pleasure to do. In particular I would like to acknowledge Dr. Karatekin for his supervision and guidance, and for all the efforts he put during the last months to help me in my research for a PhD that would suit my needs. Deep inside my heart I seriously hope that one day we will meet again as colleagues. Thanks even to Dr. Bolsée, M. Sc. Ir. Cisneros, Ing. Caldiero and Ing. Van Hove for all the help and the unforgettable experiences I had in their company. Thanks to Prof. Hubert and Prof. Grodent, for having been my internal supervisors and having helped me to arrive at this point of my career. Finally, thanks to all the amazing professors I had the pleasure to have courses with: if one day I will be able to fulfill my dreams and become a researcher it will be thanks to you all!

For the personal acknowledgements, instead, my first thought goes to my parents. You supported me for all my life and making you proud of me has always been one of my greatest joys. You made a lot of sacrifices to let me become the person that I am today, and I hope that one day I will be able to prove you all the love and gratitude that I feel for you two.

Mom, despite our occasional disagreements, your unconditional love has always represented for me a beacon of happiness to guide me in my darkest and saddest days. And dad, thank you for all the effort you put in reminding me my roots and in your genuine appreciation for the man I became; it means a lot for me.

My second thought goes to my brother, Edoardo. You always were the first person that believed in me, even when I didn't. If I ever accomplished something important in my life, you get most of the credit for that. For all my life I've always looked at you as the living proof that everything was possible if one believed enough in himself. Thank you, for having shown to a shy kid that used to cry every time his mother was leaving home, that the World is not meant to be feared, but to be embraced and experienced at its fullest. Thanks, for having been for all my life not only my big brother, but even a friend, a rival, and my constant inspiration.

I would like to also thank my cats, Oppenheimer and Marie. Thanks not only for the company, the scars and the funny anecdotes to tell other cat lovers, but even for helping me discover a part of myself that made me a better person.

My love goes to the rest of my family as well; your pride and support are the best gift that I receive every Christmas when I come back home. In particular, thanks to my cousins Francesco and Chiara, who always remained close to me despite the distances that separated each other, and thanks to my grandaunt and granduncle Anita and Ernesto, who never stopped treating me as one of their grandsons.

Thanks even to Nicola, who, in addition to be a very good friend, he has always been like my second big brother. A lot of wonderful experiences have been added to my list of most treasured memories thanks to you, Nico.

For the Italian side I would like to thank all my friends from high-school, university and anywhere else for the wonderful company and support that will never be forgotten. A special thanks goes to Marco, whose priceless friendship was of a great help in the moments of my life when I most needed a friend, and with whom I shared unforgettable moments of joy and amusement.

For the Belgian side I would firstly like to thank Elisa, Alfonso, Greg, Elena, Kawtar and Kevin for the best company I could have ever wished for during my internship at the observatory, and for all the unforgettable moments that we passed together.

Thanks then to all the people that made these two latest years the best period of my life (so far), like Charlotte, who has been a wonderful roommate, a fantastic person to converse with and a magical drinking buddy.

I would finally like to dedicate my final words to the two people I spent most of my time with during my residence in Liège and that I consider more like sisters than friends: Irene and Mari-Liis.

Irene, as I will never fail to mention you are an amazing woman who makes everyone's life more vibrant. I'm glad that we got so close and that we shared so much. When I arrived in Belgium and I didn't know any word of French, you were the only francophone that didn't feel uncomfortable in talking English with me. I've never felt alone with you around, and that is something that I will never forget. I'm sure one day the whole world will look at you as the wonderful person I always see when I am in your company.

Mari, you were the first friend I had when I moved to Belgium, and you will always have a special place in my heart. In the first months after we moved to Liège we supported each other in a world that wasn't very comfortable in interacting with us. In two years we shared the same amount of experiences that I would have normally shared in a decade with anybody else. When I will be older and I will start to sadly walk down the memory lane, I will welcome even the memories about the most difficult times of our friendship as a bliss, because I learned, from all the friends and relatives I thanked so far, that it doesn't matter how much you are different from someone, how many times you fight with someone or how far you are from someone. What truly matters is that, in the end, there will still be enough love to acknowledge how special your beloved ones are.

Thank you all for teaching me the most important lesson of all